JOURNAL OF GEOPHYSICAL RESEARCH, VOL. 102, NO. D22, PAGES 26,191–26,216, NOVEMBER 27, 1997

Equatorial dynamics observed by rocket, radar, and satellite during the CADRE/MALTED campaign 2. Mean and wave structures, coherence, and variability

David C. Fritts,[1,2] James F. Garten,[1] Dennis M. Riggin,[1,2] Richard A. Goldberg,[3] Gerald A. Lehmacher,[3] Frank J. Schmidlin,[4] Sean McCarthy,[4] Erhan Kudeki,[5] Clinton D. Fawcett,[5] Mathew H. Hitchman,[6] Ruth S. Lieberman,[7] Iain M. Reid,[8] and Robert A. Vincent[8]

Abstract. We present an analysis of the wind and temperature measurements made by rocket, radar, and satellite instrumentation in the equatorial and subtropical middle atmosphere accompanying the MALTED/CADRE campaign conducted at Alcantara, Brazil during August 1994. Measured mean winds and temperatures extended from ~10 to 110 km, exhibited general consistency between instruments, and revealed an oscillatory nature of the mean zonal wind with altitude at equatorial latitudes. MF radar measurements of tidal structures showed these to exhibit variability on ~8- and 16-day periods, but to be largely uncorrelated in time. Two-day wave structures displayed the same periodicities, but were well correlated among sites at northern and equatorial latitudes. Rocket and radar measurements at smaller scales of motion revealed inertia-gravity waves having significant temporal coherence, quadrature correlations between components indicating clear directions of propagation, and momentum flux and mean wind correlations indicative of gravity wave filtering processes. Rocket estimates of diurnal tidal amplitudes suggest that the diurnal tide achieves convectively unstable amplitudes in the upper equatorial mesosphere.

1. Introduction

The Coupling And Dynamics of Regions Equatorial (CADRE) measurement campaign series was conceived to enable comprehensive studies of equatorial coupling, dynamics, structure, and variability in the equatorial and subtropical middle atmosphere. CADRE science objectives helped to focus measurement activities and provide additional instrumentation for selected measurement periods. The result was a combination of radar, balloon, rocket, and satellite measurements which provided unique opportunities for correlative analyses. An overview of the initial CADRE campaign objectives and of the correlative efforts that are collected in this special section is provided by *Fritts* [this issue]. The purpose of this paper is to use correlative data sets at various sites to examine the structure and variability of the mean, large-scale, and smaller-scale motion fields during the CADRE/Mesosphere And Lower Thermosphere Energetics and Dynamics (MALTED) rocket and radar campaign. This campaign comprised one of the core CADRE intervals and as such also benefitted from other correlative measurement capabilities not specifically committed to these campaign objectives. An overview of the MALTED campaign, a discussion of the data acquisition and analysis procedures, and inferences of small-scale turbulence activity associated with larger-scale wave motions are provided in a companion paper by *Goldberg et al.* [this issue].

The equatorial lower and middle atmosphere hosts a wide range of dynamical processes, many or all of which are dynamically coupled in ways that are only beginning to be understood. Zonal mean equatorial motions experience oscillations exhibiting periodic or quasi-periodic behavior due to a combination of wave

[1]Colorado Research Associates/NWRA, Boulder.
[2]Also at Program in Atmospheric and Oceanic Sciences, University of Colorado, Boulder, Colorado.
[3]Laboratory for Extraterrestrial Physics, NASA Goddard Space Flight Center, Greenbelt, Maryland.
[4]Wallops Flight Facility, NASA Goddard Space Flight Center, Wallops Island, Virginia.
[5]Department of Electrical and Computer Engineering, University of Illinois, Urbana.
[6]Department of Atmospheric and Oceanic Sciences, University of Wisconsin-Madison.
[7]Space Physics Research Laboratory, University of Michigan, Ann Arbor.
[8]Department of Physics and Mathematical Physics, University of Adelaide, Adelaide, South Australia.

Paper number 96JD03966.
0148-0227/97/96JD-03966$09.00

and mean transports of momentum at large and small scales. The quasi-biennial oscillation (QBO) in the equatorial lower and middle stratosphere is believed to derive its forcing primarily via Kelvin and inertia-gravity wave (IGW) propagation and dissipation in its eastward phase [*Takahashi and Kumakura,* 1995]. Its westward phase appears to be driven by a mixture of IGWs, Mixed Rossby-gravity waves, extratropical planetary waves, and mean meridional advection. Indeed, it is now understood that these primarily wave-driven circulations also account for both the downward descent and period of the QBO and the mean upwelling observed at equatorial latitudes acting to decrease the rate of QBO phase descent [*Plumb and McEwan,* 1978; *Plumb and Bell,* 1982; *Dunkerton,* this issue; *Sato and Dunkerton,* this issue]. Extratropical QBO correlations have also been noted by a number of authors, suggesting that this equatorial oscillation influences the global atmospheric circulation and structure in important ways [*Holton and Tan,* 1980, 1982; *O'Sullivan and Salby,* 1989].

In contrast to the QBO, the semiannual oscillation (SAO) has a period that is phase-locked to the annual cycle and exhibits zonal wind maxima near the stratopause and mesopause which are in approximate antiphase [*Hirota,* 1978; *Dunkerton,* 1982]. Also observed are a stronger first cycle each year, significant extensions of the mesospheric SAO into subtropical latitudes, and a tendency for a westward mean due to meridional and vertical momentum transports [*Hamilton,* 1982; *Hitchman and Leovy,* 1986; *Delisi and Dunkerton,* 1988; *Fritts and Isler,* 1994; *Garcia et al.,* this issue]. The stratopause and mesopause SAO (SSAO and MSAO) owe their existence largely to those equatorial wave motions having larger horizontal phase speeds and vertical group velocities, primarily gravity waves and fast (lower zonal wavenumber, large vertical wavelength) Kelvin waves. Evidence for such motions at these altitudes was provided, for example, by the Jicamarca mesosphere-stratosphere-troposphere (MST) radar in Peru and the medium frequency (MF) radar at Christmas Island [*Vincent and Lesicar,* 1991; Fritts et al., 1992; Hitchman et al., 1992], by previous balloon, rocket, and satellite observations [*Eckermann,* 1995; *Eckermann et al.,* 1995], and in this collection of CADRE papers by *Riggin et al.* [this issue a,b], *Sato and Dunkerton* [this issue], *Shiotani et al.* [this issue], and *Lieberman and Riggin* [this issue]. The tendencies here are for statistically slow and systematic wave forcing because of the small accelerations needed to account for the SAO structures.

At greater altitudes, gravity wave and tidal forcing play increasing roles individually and in concert. The diurnal tide contributes a net westward acceleration above ~80 km at equatorial latitudes [*Lieberman and Hays,* 1994], while gravity waves contribute locally large fluxes which appear to be modulated by and correlate highly with the tidal structures. Like the interactions observed at other locations [*Fritts and Vincent,* 1987; Wang and Fritts, 1991], gravity wave/tidal interactions also appear to play important roles in equatorial and subtropical dynamics. A related CADRE study by *Nakamura et al.* [this issue] showed gravity wave-tidal interactions inferred from tidal amplitude and phase variability to be consistent with the model proposed by *Fritts and Vincent* [1987]. Recent results with the NCAR TIME GCM suggest that gravity wave/tidal interactions have important implications for forcing of the mean flow as well, with mean flow responses being quite different with and without gravity wave influences included. The results are promising in this case, with a self-consistent mean flow predicted by the TIME GCM model in excellent agreement with observations of the zonal mean circulation inferred by the HRDI and WINDII instruments aboard UARS [*McLandress et al.,* 1996; *R. Roble,* private communication, 1996]. Importantly, observations and model results exhibit a westward zonal wind at ~85 km during equinoctial conditions due to tidal forcing which may play a role in the westward phase of the MSAO, particularly during March and April when tidal amplitudes are a maximum [*Garcia et al.,* this issue].

Our objectives in this paper are several. We first examine in section 2 the meteorological rocket wind and temperature data to determine data quality and what features represent real atmospheric fluctuations. In section 3 we define the mean and low-frequency character of the lower and middle atmosphere mean wind fields during the August 1994 CADRE campaign. This effort utilizes rocket data collected at Alcantara, Brazil during the CADRE/MALTED campaign, radar data spanning a range of equatorial and subtropical latitudes, and HRDI data extending to 70°N and 70°S. Diurnal tide and 2-day wave winds and temperatures and their variability are examined and intercompared in section 4. Section 5 examines the character of the motion field at smaller scales, the relations between zonal and meridional velocities, the momentum fluxes accompanying these motions, and their correlations with the local mean winds and shears. Our results are summarized in section 6.

2. Rocket Data Analysis and Discussion

As described by *Goldberg et al.* [this issue], MALTED consisted of a series of 20 falling sphere payloads flown aboard Viper meteorological rockets (MR) and four Nike-Orion sounding rockets instrumented for small-scale structure measurements. All rockets were flown from Alcantara, Brazil located on the coast at 2° S. A map showing the locations of this site and of the MF radars and the Jicamarca MST radar, also used for this study, is shown in Figure 1 of *Goldberg et al.* [this issue]. Of the falling sphere payloads, 15 were flown and successfully deployed and tracked by either or both the Brazilian Atlas and NASA tracking radars. These

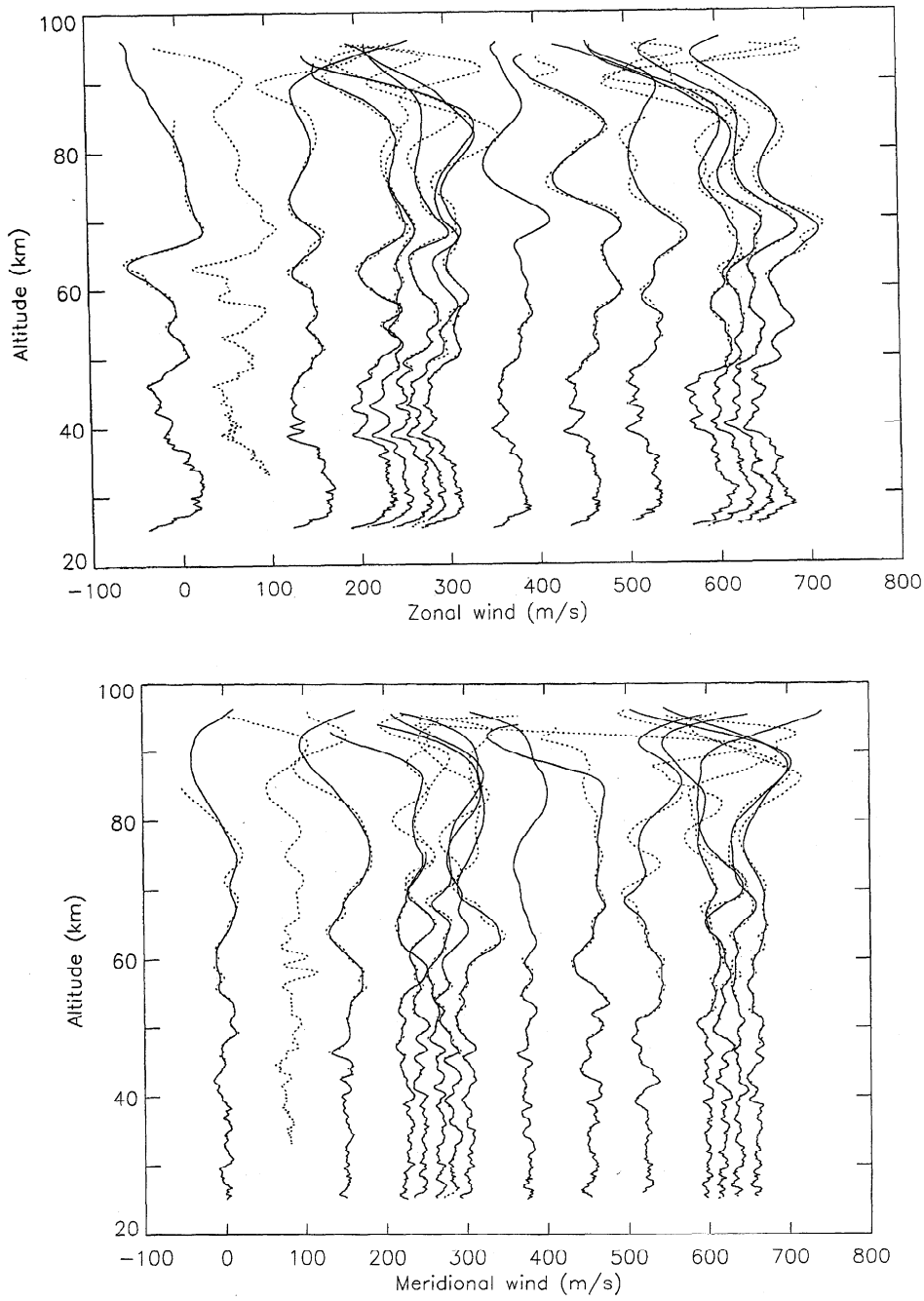

Figure 1. Zonal (top) and meridional (bottom) wind measurements using meteorological rockets with Atlas/Brazilian (solid) and NASA (dashed) tracking systems. Successive profiles are displaced by 75 m s^{-1} per 24-hour interval. Wind estimates in each case were made using the narrow 29/21 filter described in the text.

high-precision radars were located ~35 km apart, obtained the falling-sphere data using different tracking algorithms, and yielded independent estimates of falling-sphere position and of the inferred velocities and accelerations with time. In each case, however, position data were recorded at 10 Hz and then averaged to 2 Hz for further processing.

To insure as much consistency as possible between data sets and to evaluate the relative uncertainties within and between data sets, each was processed to determine winds and temperatures in the same manner. For wind determinations, the inferred velocity and acceleration data were subjected to a filter using 29 velocity and 21 acceleration estimates (denoted a 29/21 filter), yielding wind estimates retaining significantly more vertical structure than the more normal 51/35 filter [*Schmidlin*, 1986]. This was done in order to avoid artificially suppressing smaller-scale structures without

first determining their relative accuracies. The zonal and meridional wind estimates obtained in this manner for each radar are shown in Figure 1 without additional vertical smoothing. Successive profiles are staggered based on their temporal spacing, with a displacement of 75 m s^{-1} per 24-hour period. The closely spaced five- and four-rocket salvoes correspond to the two key days during which the sounding rockets were also launched.

The Atlas (solid) and NASA (dashed) wind determinations shown in Figure 1 are seen to be in excellent agreement at altitudes up to ~60 km in all cases, with generally good agreement to ~80 km in most instances, and occasionally reasonable agreement to ~90 km. More specifically, the Atlas and NASA wind estimates are virtually indistinguishable at lower levels, with small-scale wind features present in both data sets for each falling sphere and displaying considerable consistency between successive profiles. This is particularly apparent in the zonal component, where we see that all profiles exhibit large-scale maxima near 30-km and 70-km altitudes and minima between ~40 and 50 km and again near or above ~60 km. At smaller scales, successive profiles display multiple maxima and minima which correlate well over several days, particularly near 40 km. Uncertainties below 40 km are a few meters per second or less, with the filtering described above imposing a vertical smoothing over ~1 km due to sampling at ~30 data points per kilometer. Above ~60 km, the larger-scale (~10 km and longer wavelengths) motions are again reasonably well correlated, though with some amplitude uncertainty and with the smaller vertical scales (~5 km and shorter wavelengths) suppressed more strongly in the NASA (dashed) than in the Atlas (solid) data. Different wind estimates and spatial scales in these two data sets exhibit the uncertainties imposed by the tracking techniques (rms uncertainties of ~5 to 10 m s^{-1} between 60 and 80 km) and the greater spatial smoothing (~2 to 3 km) due to sampling at ~10 data points per kilometer at greater altitudes. Thus, wind estimates are not considered valid above ~90 km due to the increasing uncertainties at these altitudes [*Schmidlin*, 1984; *Schmidlin et al.*, 1985].

Temperature profiles were obtained in a similar manner, but using 17 velocity and 19 acceleration values for density estimates and, assuming a hydrostatic atmosphere, integrating downward from a reference temperature at the acquisition altitude (above 90 km). Additionally, we found the Atlas temperature profiles to exhibit considerably more small-scale structure than those obtained with the NASA tracking system because of the operational configuration of the Atlas system. To suppress the temperature differences introduced by the different tracking schemes, we also employed a triangular weighted vertical smoothing with a full width at half maximum of 3 km. The resulting temperature profiles for those soundings for which both radars were operational are shown together in Figure 2. While there is considerably less vertical structure at small scales than present in the wind profiles, the larger-scale features in these profiles compare well up to altitudes of ~80 km in most cases, with this agreement extending to ~90 km in a few instances. Like the wind data, temperatures are not considered valid above ~90 km because of the increasing uncertainties at these altitudes.

As noted for the velocity data, the temperature data also display features at large and intermediate scales

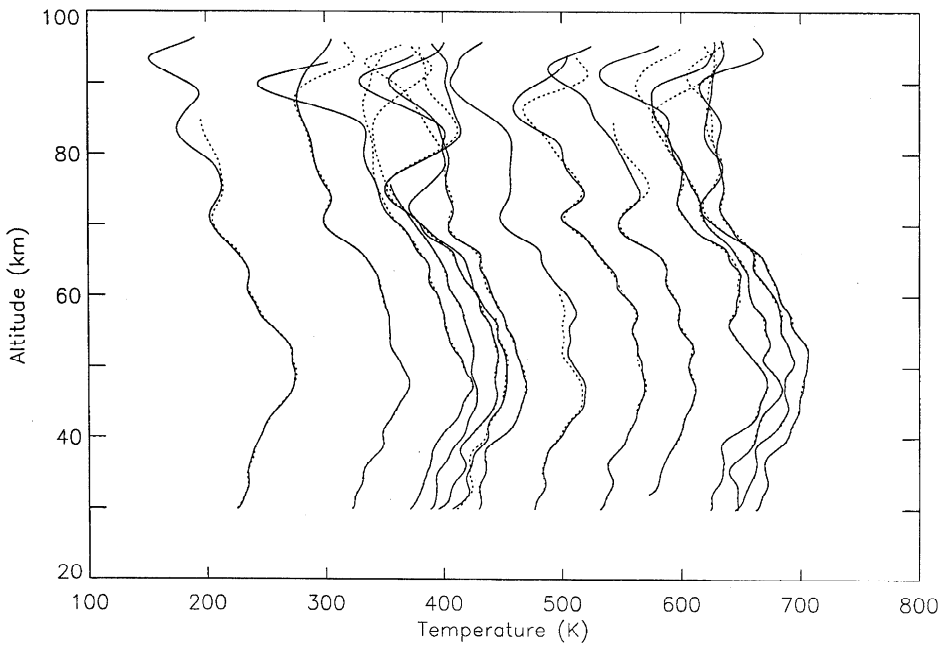

Figure 2. As in Figure 1, but for the temperature profiles using the 17/19 filter and a 6-km triangular smoothing to further suppress differences between the two profiles in each case.

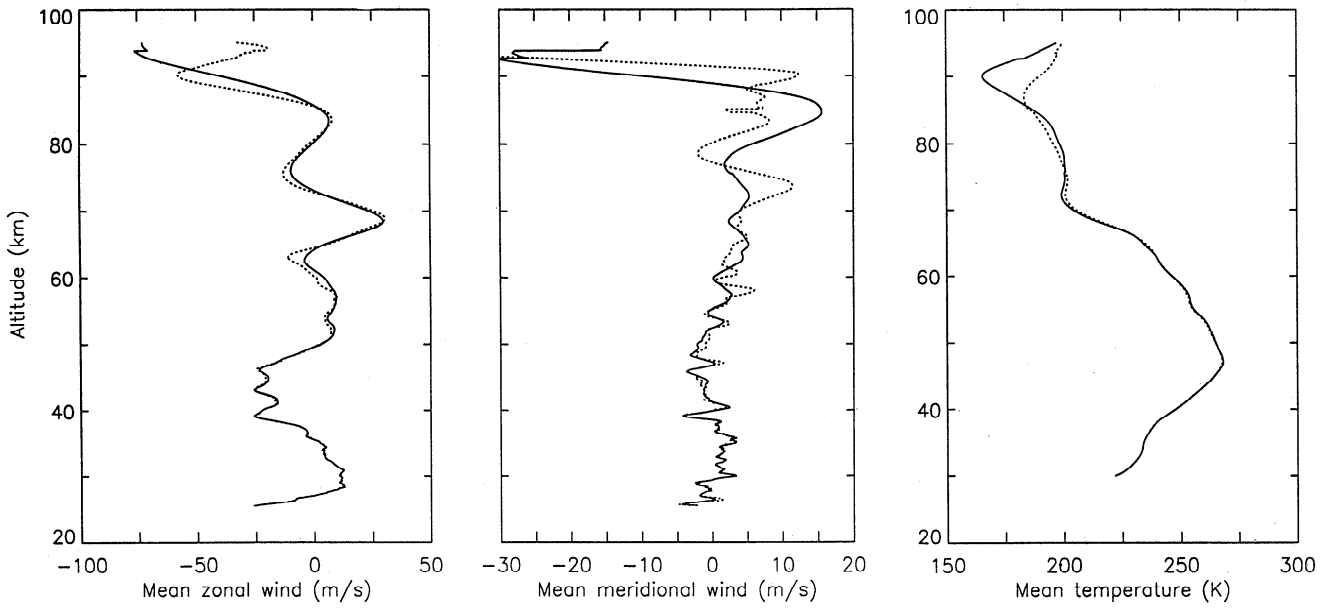

Figure 3. Mean zonal (left) and meridional (center) winds and temperatures (right) obtained by averaging all meteorological rocket data from the Atlas (solid) and NASA (dashed) tracking systems displayed in Figures 1 and 2.

that are persistent between adjacent profiles. The most conspicuous features are the maximum near the stratopause (~50 km) and the minimum near the mesopause (~90 km). There are, nevertheless, other features that also persist for several days or which exhibit distinct variations with time. These include the local temperature minimum near 70 km between the two key days and the large and diurnally-variable fluctuations above ~80 km.

3. Mean Winds and Low-Frequency Variability

We now employ the rocket and correlative satellite and radar data sets to examine the mean and low-frequency wind and temperature structures present during the August 1994 CADRE campaign. Mean wind and temperature profiles for the MR data were computed by averaging all of the individual profiles to-

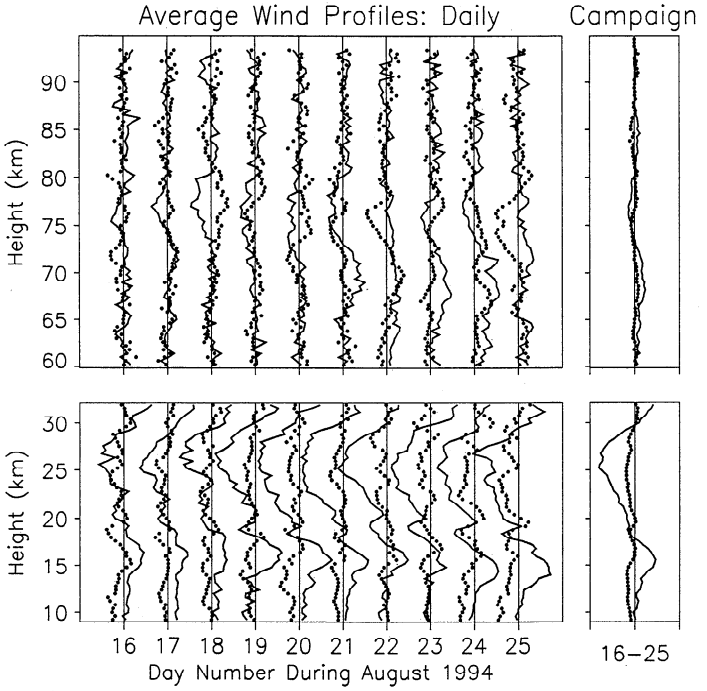

Figure 4. Daily and campaign mean zonal (solid) and meridional (dots) winds obtained in the troposphere and lower stratosphere (lower panels) and mesosphere (upper panels) with the Jicamarca MST radar during the MALTED campaign. Successive profiles are offset by 20 m s^{-1}.

gether. These profiles represent means from August 16 to 24 and are shown in Figure 3 using the same line designations as above. Because the daily launches occurred near 1100 LT each day, however, there is a potential for a bias of the mean profiles by the tidal structures where tidal amplitudes are large (above ~80 km, see below).

The Jicamarca MST radar was operated in support of the MALTED rocket campaign and obtained wind measurements simultaneously in the upper troposphere, lower stratosphere, and mesosphere during daytime. Daily and campaign mean zonal and meridional winds for this data set are displayed as solid and dotted profiles in Figure 4. Like the rocket data, however, daytime only measurements introduce the possibility of tidal contamination of the mean profiles at greater altitudes. Apart from tidal influences, we estimate uncertainties in daily mean winds to be ~3 m s^{-1} or less in the stratosphere and mesosphere, except above ~85 km, where pulse coding and electrojet contamination at greater altitudes likely result in increasing underestimates of the winds with increasing altitude.

A mean zonal wind profile for August 1994 was also computed with measurements from the High Resolution Doppler Imager (HRDI) instrument aboard UARS [*Hays et al.,* 1993] in support of the August CADRE campaign. In this case, a monthly mean is necessary to average over all local times and suppress tidal contamination of the inferred mean winds. This cross section, extending from 65 to 110 km altitude and from 70° S to 70° N, is shown in Figure 5.

Finally, time-height cross sections of the low-pass zonal and meridional winds for the Hawaii, Christmas Island, and Adelaide MF radars during August 1994 are shown in the upper and lower panels of Figures 6, 7, and 8. These winds represent two-day-long means slid by 12 hours in order to average over tidal and 2-day wave contributions. The upper time series and the vertical profile at the right edge display the altitude and time averages of the data in each case. Zonal and meridional winds at Christmas Island are also displayed at higher resolution (daily means slid by 6 hours) for the ten days of the MALTED rocket campaign (16 to 26 August 1994) in Figure 9. Wind measurement uncertainties for these systems have been discussed previously by Vincent and Lesicar (1991) and Fritts and Isler (1994) and are typically ~5 m s^{-1} for hourly averages at altitudes with higher data rates and somewhat larger above and below.

3.1. Mean Winds and Trends

Comparison of the various mean wind profiles shown in Figures 3–8 reveals clear strengths and limitations of the various data sets. The rocket data, for example, while very limited in its temporal resolution, are the only data set that extends continuously throughout the stratosphere and mesosphere. Measurements with the Jicamarca MST radar link the troposphere and lower stratosphere and permit momentum flux estimates at lower and upper levels, but provide no data between ~35 and 60 km altitudes. Likewise, HRDI measurements are global, but provide no temporal variability or nighttime measurement capabilities except near 95 km. Finally, MF radars yield nearly continuous hori-

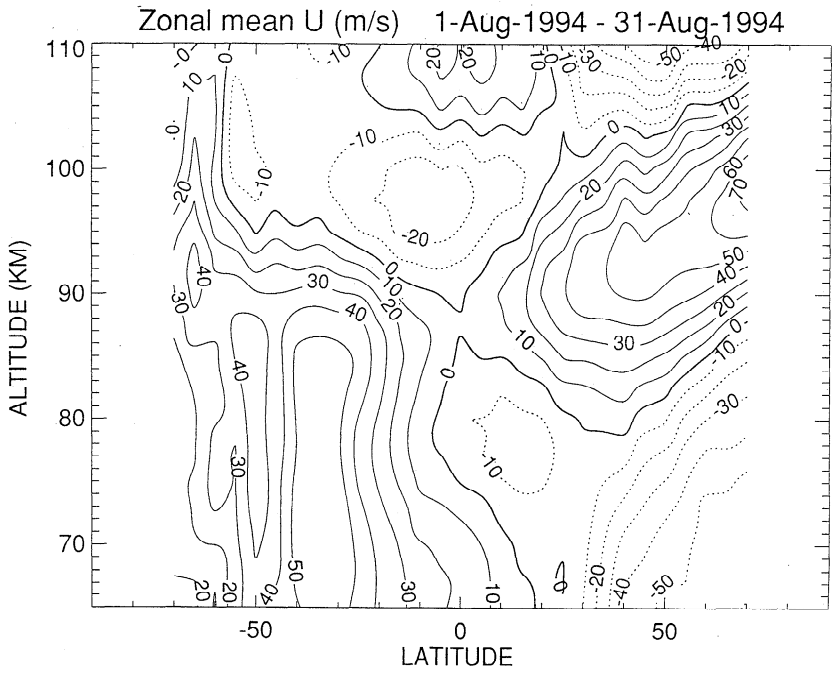

Figure 5. Monthly mean zonal wind cross section for August 1994 inferred from HRDI wind measurements aboard UARS. Solid (dashed) contours are eastward (westward) and contour intervals are 10 m s^{-1}.

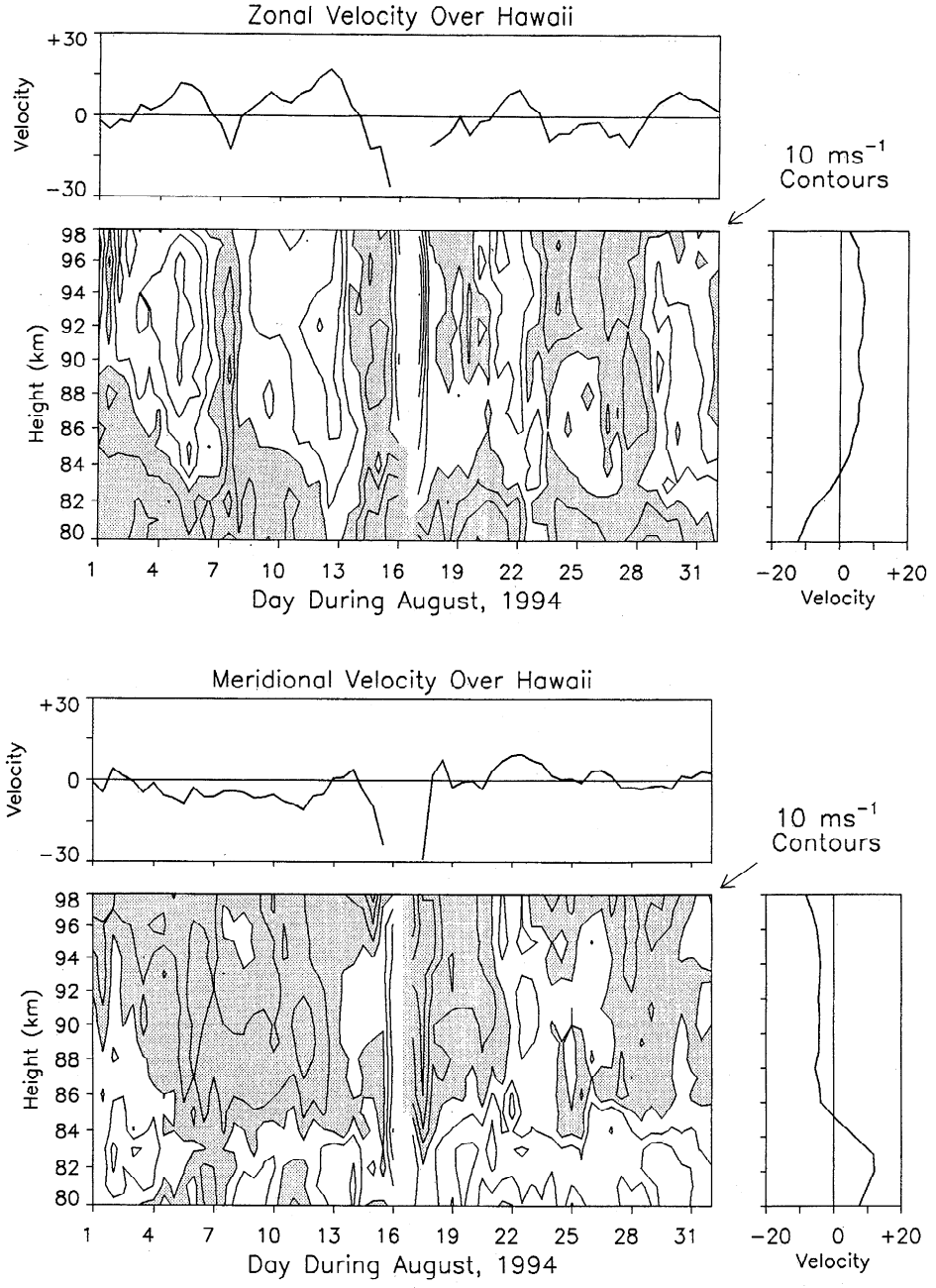

Figure 6. Zonal (top) and meridional (bottom) winds inferred for two-day-long intervals slid by 12 hours for August 1994 with the MF radar at Hawaii. Shading denotes westward or southward winds and contour intervals are 10 m s^{-1}. The upper time series and vertical profiles represent vertical and time averages in each case.

zontal wind measurements, but they are restricted to greater altitudes, do not provide momentum flux estimates, and do not permit a simple decomposition of the various motions comprising the motion spectrum. As such, each data set has advantages and limitations which insure the greatest analysis potential when using these data in a correlative analysis effort.

At the lowest altitudes, the Jicamarca radar and rocket data suggest an oscillatory mean zonal wind with altitude, with eastward motions below ~18 km, westward mean motions between ~18 and 28 km, eastward motions between ~28 and 35 km, westward motions again from ~35 to 50 km, and generally weak eastward motions extending from ~50 to above 70 km. These data also are consistent with the ECMWF analysis for August 1994 (not shown), which displays eastward motions below ~17 km and above ~28 km and westward motions at intermediate altitudes during the MALTED campaign. Mean meridional motions at lower levels tend to be much smaller, with weak southward motions suggested by both rocket and radar profiles below 30 km and small northward motions between ~30 and 40 km

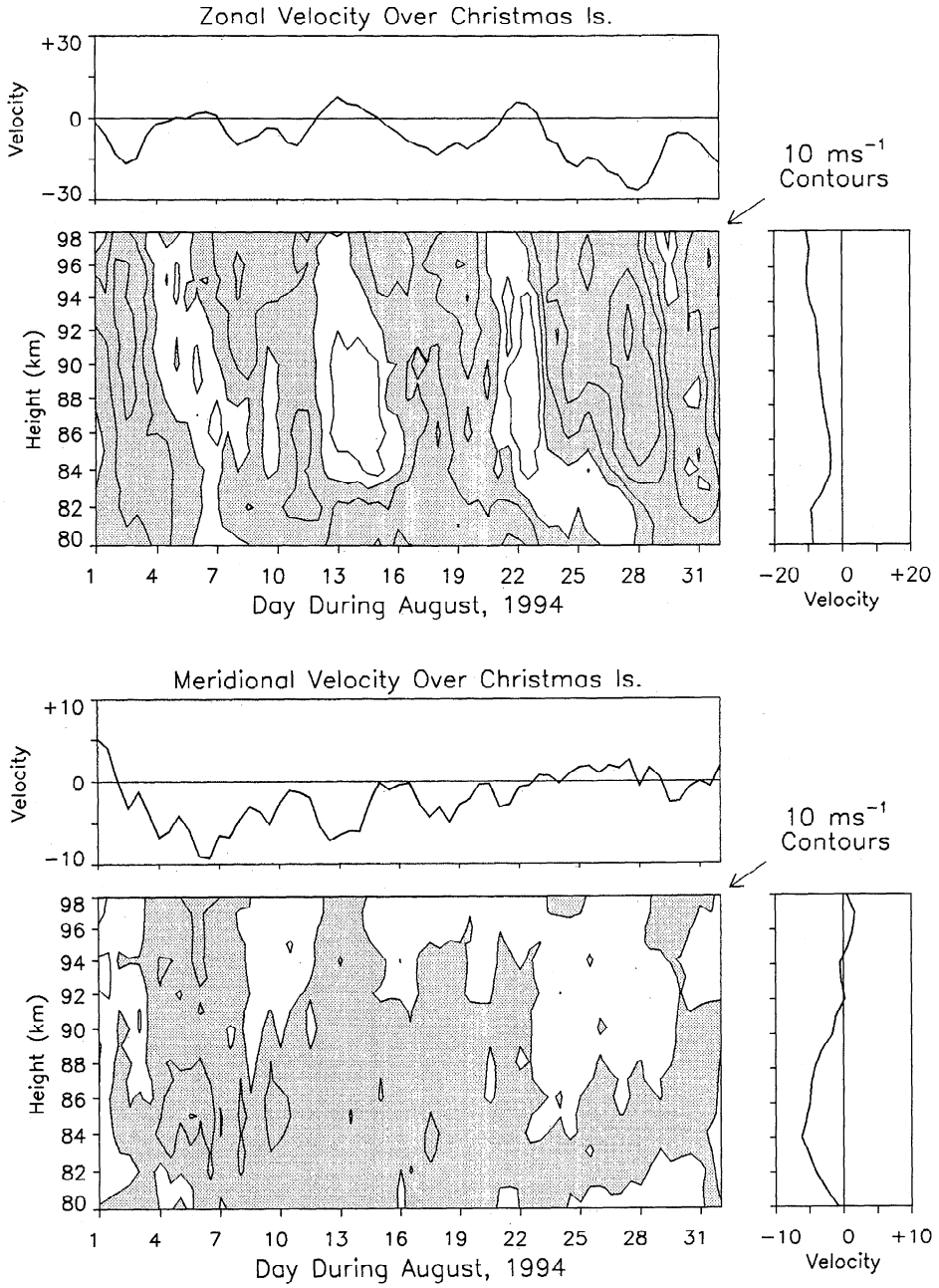

Figure 7. As in Figure 6, but for the Christmas Island MF radar.

and again above ~50 km apparent in the rocket mean winds.

Referring now to the rocket and HRDI data shown in Figures 3 and 5, we see that the mean zonal winds are also variable with height at greater altitudes, though to a smaller degree than at lower altitudes. Both rocket and HRDI mean winds reveal an equatorial eastward flow near and below 70 km, weak westward motions centered below ~80 km, a second altitude range with weak eastward motions below 90 km, and increasing westward winds to a maximum between ~95 and 100 km. At greater altitudes, the HRDI data reveal a clear eastward wind at 110 km and above which is suggestive of the equinoctial zonal mean measured by HRDI and WINDII and simulated in the TIME GCM [*McLandress et al.*, 1996; *R. Roble*, private communication, 1996]. Similar zonal maxima are also seen at lower levels in the Jicamarca mean winds, though the magnitudes are typically smaller than observed in the rocket or HRDI data. There are, of course, differences between these profiles when examined in detail. As examples, the zonal wind maximum below 70 km is considerably stronger in the rocket wind profile than in the HRDI monthly mean, while the negative and positive maxima at greater altitudes are both larger in magnitude and displaced downward in the rocket data compared to the HRDI wind

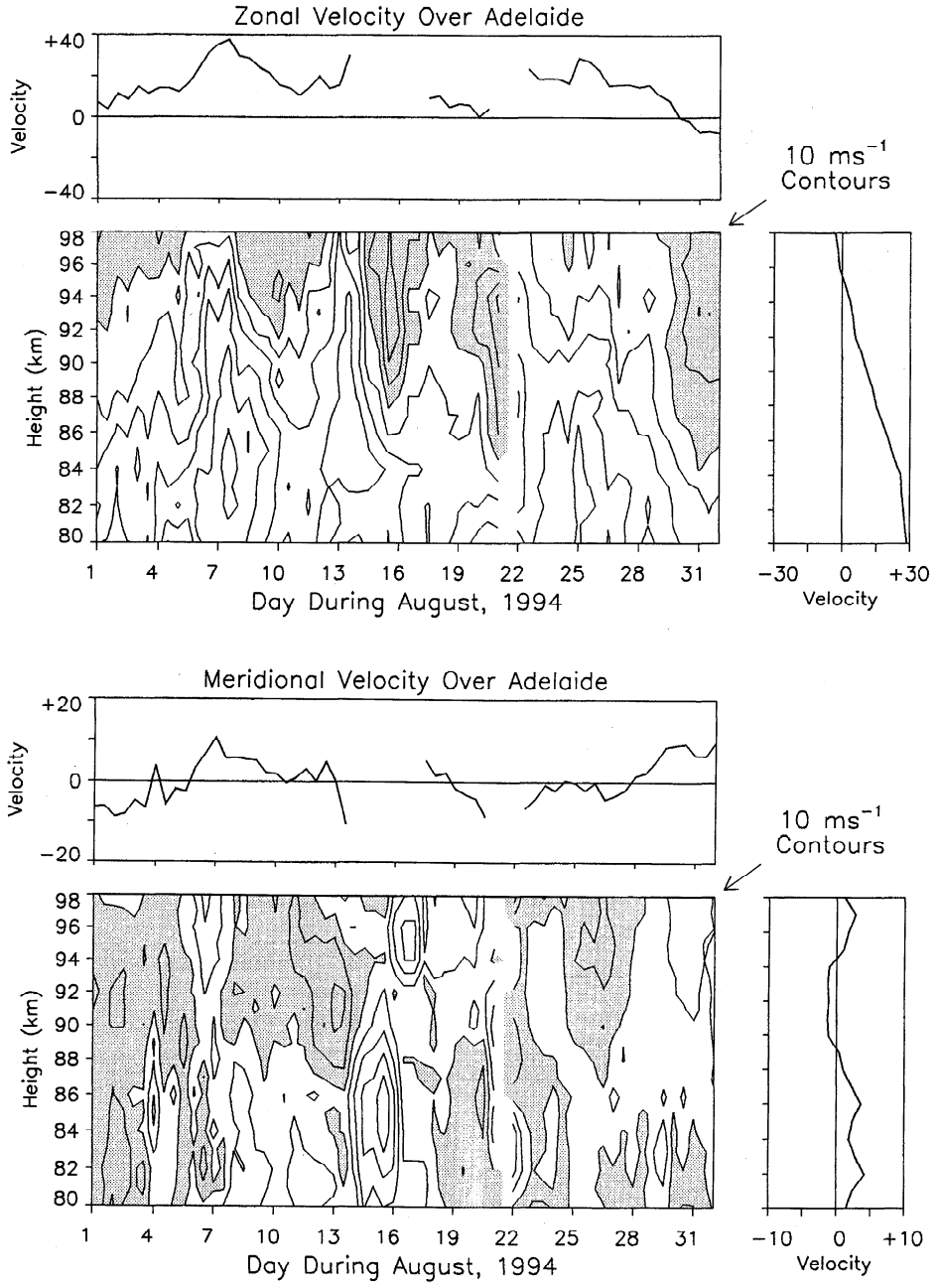

Figure 8. As in Figure 6, but for the Adelaide MF radar.

field. The agreement is nevertheless striking considering the different averaging intervals and the limited number of rocket profiles comprising the average.

Turning now to the MF radar monthly mean zonal winds (right upper panels in Figures 6, 7, and 8), we see that these mean profiles also correlate reasonably with the zonally-averaged mean zonal wind obtained by HRDI. In the case of the Hawaii data we see a transition from westward mean motion below ~84 km to eastward mean motion at greater heights which compares well with the HRDI mean zonal winds in sign but is smaller in magnitude by a factor of ~2 near 90 km. A similar tendency is seen in the mean wind profile at Christmas Island, where westward winds predominate, except for values closer to zero at intermediate altitudes. In this case, the magnitudes of the westward winds appear to agree reasonably well between the two data sets. Finally, we note a tendency at Adelaide for the zonal mean wind to decrease from large positive values at lower levels through zero near 96 km in both data sets. As above, there are many features common to these data sets which suggest that they each provide a reasonable, if not perfect, view of the mean motion field. As noted at lower levels, mean meridional motions at greater altitudes remain small, with weak northward winds from ~50 to 90 km altitude implied by the rocket

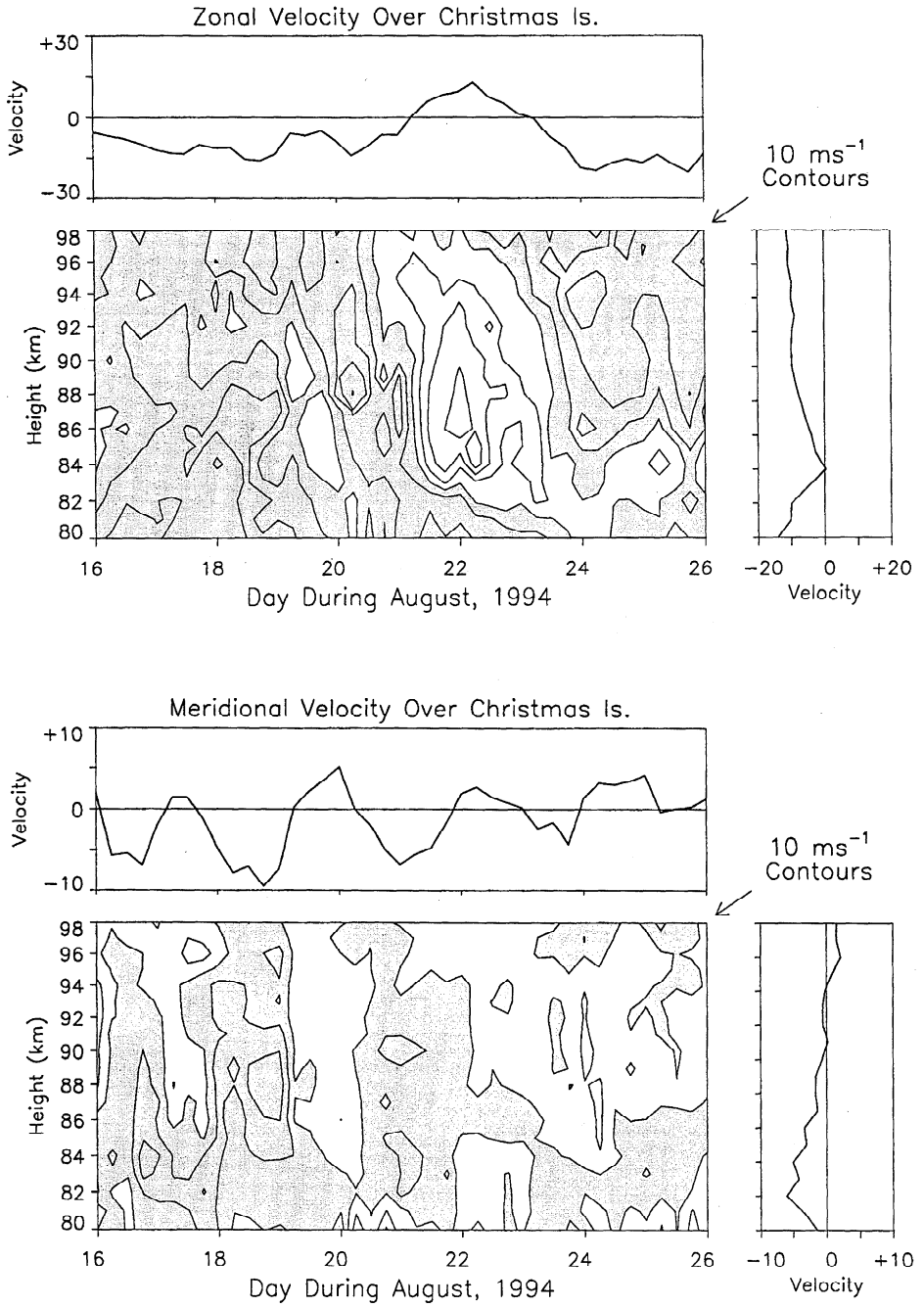

Figure 9. As in Figure 6, but for two-day-long intervals slid by 6 hours from August 16 to 26 1994 for the Christmas Island MF radar.

data and weak, though variable, winds in the MF radar data.

We now note that the mean zonal winds measured during the MALTED campaign in the lower stratosphere are consistent with the amplitudes and phase descent of the QBO at this time [*Hitchman et al.*, this issue]. The lack of significant zonal winds at stratopause and mesopause altitudes is likewise consistent with seasonal variations in the SSAO and MSAO amplitudes, which are typically near a minimum during August [*Hirota*, 1978; *Garcia et al.*, this issue].

3.2. Planetary Wave Structures and Variability

We now examine the variability of the zonal and meridional winds on planetary wave (longer than 2-day) timescales at the time of the MALTED campaign. Only the MF radar data are used for this purpose, as the rocket and Jicamarca data are available only during the 10-day campaign interval. UARS data likewise yield no planetary wave structures without fitting discrete zonal wavenumber and frequency components.

The most conspicuous structures in the height-averaged time series for each radar (see the upper panels

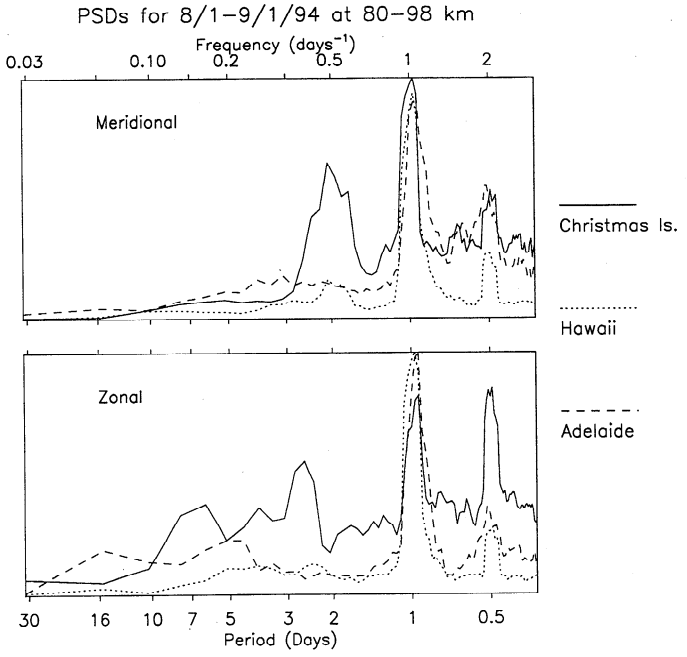

Figure 10. Semilog frequency spectra in variance-content form, $\omega F(\omega)$, of 4-hour averaged (top) meridional and (middle) zonal winds measured by the MF radars at Christmas Island (solid), Hawaii (short dashed), and Adelaide (long dashed) during August 1994. All spectra are displayed with the same amplitude scale, and the diurnal amplitude peak at Hawaii is twice the maximum amplitude shown in the zonal plot and 1.86 times the maximum in the meridional plot. Also shown (bottom) panel are 90% confidence limits as a function of frequency.

in Figures 6–8) are ~4- to 8-day oscillations of the zonal winds. An ~8-day oscillation is especially apparent in the zonal wind cross section from Christmas Island, where we observe a tendency for downward phase progression with time. A corresponding zonal motion is seen to occur at Hawaii and Adelaide with approximately the same phase and amplitude (~10 to 20 m s^{-1}) during the first half of the month. Each of the cross sections also exhibits variability on shorter time scales as well, with a superposed ~4-day motion apparent at Christmas Island and somewhat more variable motions at Hawaii and Adelaide. The meridional winds, in contrast, display much less variability, with only Adelaide indicating motions having ~3- to 5-day periods. These higher-frequency motions also exhibit a tendency for downward phase progression with time. In all cases, rapid phase descent suggests relatively long vertical wavelengths of ~50 km or more above ~85 km.

To examine the equatorial wave structures at higher frequencies more closely, we display in Figure 9 the daily-averaged Christmas Island winds at 6-hour intervals. As above, the time series and vertical profile represent height and time averages of these data. Variance-content frequency spectra of the zonal and meridional winds at each radar averaged for four hours are shown in Figure 10.

The dominant feature of the zonal wind field at Christmas Island during the MALTED campaign was the ~8-day oscillation exhibiting an eastward maximum of ~20 m s^{-1} between ~84 and 90 km on August 22. This maximum is approximately twice the magnitude suggested by the zonal wind cross section shown in Figure 7 because of the smaller temporal averaging of the data in this case. It also corresponds in time and height to the eastward maxima seen above 80 km in the two daily rocket wind profiles following the first key-day sequence in Figure 1. Thus, it is apparent that not all of the features seen in the daily rocket wind (and temperature) profiles can be attributed to tidal structures, and we must be careful to infer these motions only in data sets having adequate temporal resolution.

Also seen in the higher-resolution data shown in Figure 9 is evidence of motions with frequencies higher than previously discussed. Both zonal and meridional time series reveal motions having periods of ~2 to 3 days, with the shorter period most pronounced in the meridional wind data. These data show the ~2-day motion to be largely confined to the earlier part of the MALTED campaign.

The zonal and meridional wind spectra shown in Figure 10 are all normalized to half the peak amplitude of the diurnal response in the zonal wind and exhibit additional peaks at all of the frequencies discussed above. Specifically, the zonal wind spectrum for Christmas Island has a significant maximum at ~2.7 days and a broader, though less significant enhancement at ~7 days. The Adelaide and Hawaii spectra likewise show significant enhancements near 5 and 16 days and from ~2 to 5 days, respectively, though the individual maxima do not have the same significance as those at higher frequencies. Meridional wind spectra, by comparison, display very little variance at periods longer than two days, thus confirming the significance of the broader enhancements in the zonal wind spectra at lower frequencies. The zonal spectral peak near ~2.7 days at Christmas Island appears to be distinct from that centered at 2 days in the Christmas Island meridional wind spectrum. If so, it is likely a signature of an equatorial Kelvin wave, as discussed by *Lieberman and Riggin* [this issue], *Shiotani et al.* [this issue], and *Riggin et al.* [this issue a]. Indeed, the period, the large vertical wavelength, and the apparent response in only the zonal wind data are all suggestive of a fast Kelvin wave with low zonal wavenumber. Variances at 2-day periods and shorter are even more significant than the planetary wave scales, and will be discussed further below.

4. Tidal and 2-Day Wave Structures

Apart from the zonal motions at planetary wave frequencies, the motions accounting for the greatest spectral variances in Figure 10 are the 2-day wave and the

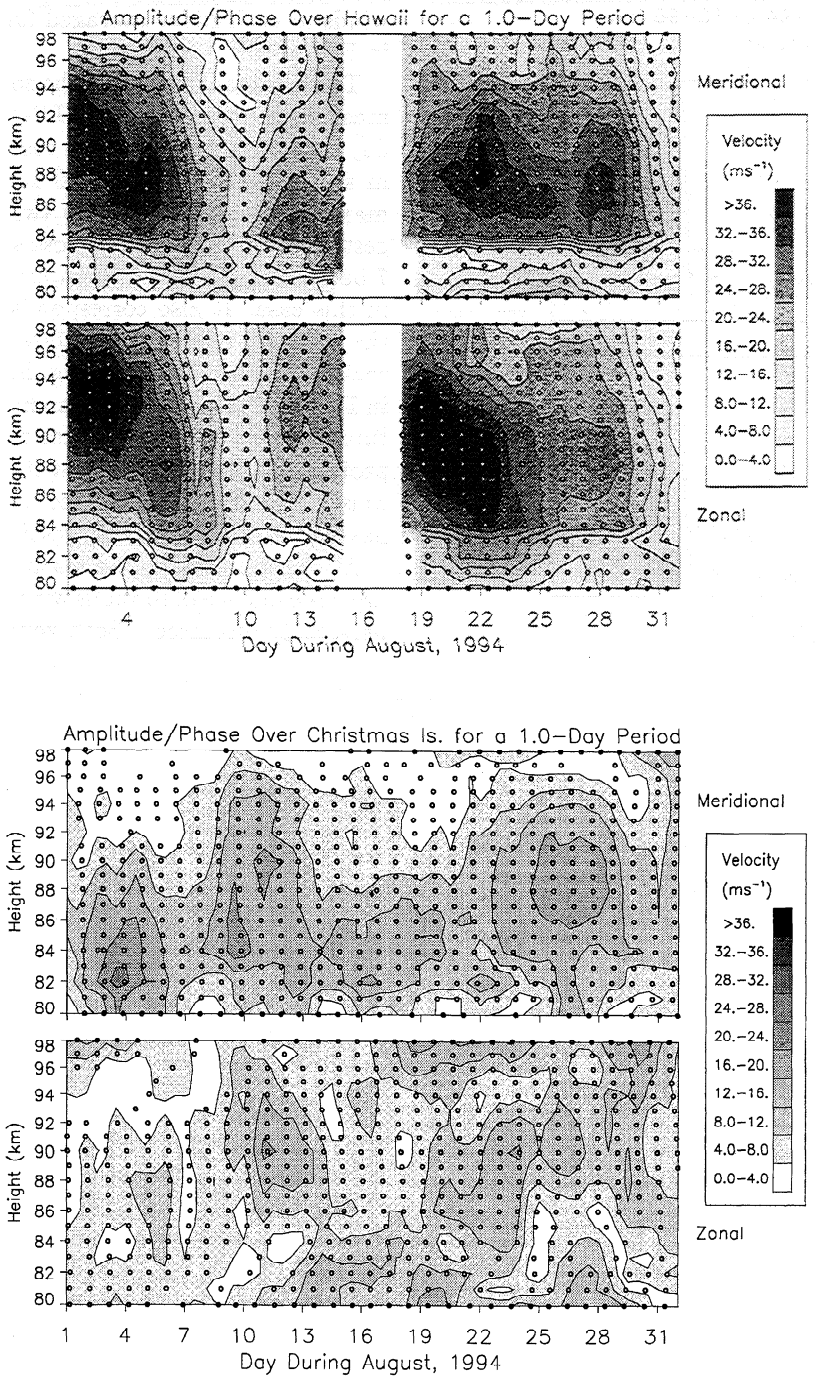

Figure 11. Diurnal tide (bottom) zonal and (top) meridional amplitude and phase estimates at (a) Hawaii, (b) Christmas Island, and (c) Adelaide during August 1994. Estimates are for 4-day intervals slid by one day and phases are displayed with circles at the time of maximum amplitude.

diurnal and semidiurnal tides. Of these, the diurnal tide makes the dominant contribution in each case, except at Christmas Island, where the 2-day wave has a very large meridional amplitude and the diurnal tide has a relatively small zonal amplitude. There, the variances of the diurnal tide and the 2-day wave or semidiurnal tide are comparable in the meridional and zonal components, respectively.

To explore the variability of the diurnal tide and the 2-day wave during the MALTED rocket campaign, we have performed fits of 24-hour and 48-hour period sinusoids to the MF radar data at each altitude. Amplitudes and phases were obtained from fits to data segments four cycles long (i.e., 4 and 8 days) which were slid in increments of 12 hours to determine the time dependence. We have also attempted fits of diurnal pe-

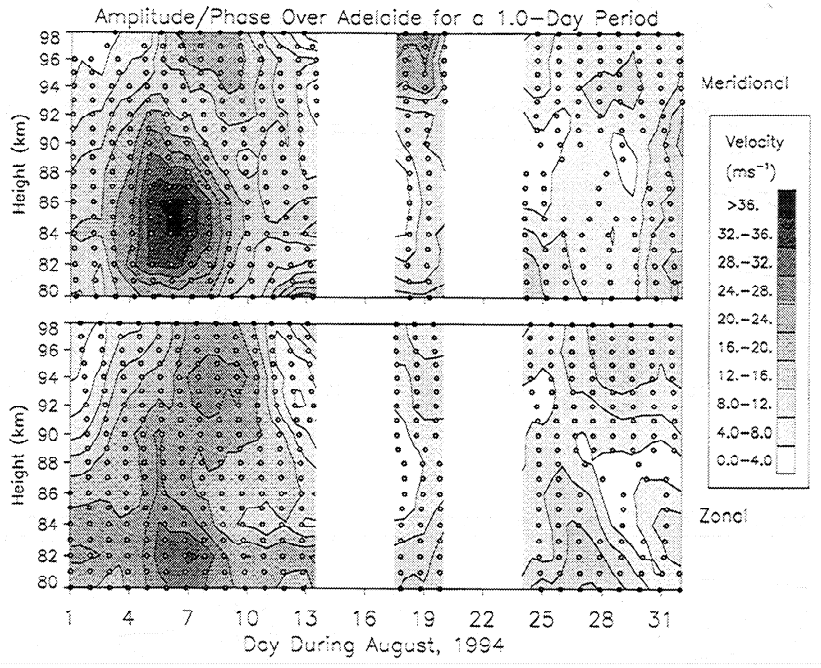

Figure 11. (continued)

riods to the two key days for which the meteorological rocket soundings provided nominal resolution of the diurnal tide. The resulting time-height cross sections of the diurnal tide amplitude for August 1994 are shown in Figure 11a, b, and c. The inferred phase variations (time of maximum amplitude) are shown for each day and each altitude with an open circle. Corresponding cross sections of the 2-day wave amplitude and phase are displayed in Figure 14a, b, and c. The diurnal fits to the rocket key-day measurements are shown in Figures 12 and 13.

4.1. Diurnal Tide Observations

Considering first the tidal amplitudes contoured in Figure 11, we see that the maximum amplitudes achieved at Hawaii and Adelaide are comparable, ~40 m s^{-1} in each case. However, larger amplitudes are more prevalent at Hawaii due to its proximity to the latitude at which the zonal wind for the symmetric zonal wavenumber 1 mode, S(1,1), is a maximum. Diurnal amplitudes at Christmas Island, by comparison, are approximately half as large. The sharp tidal amplitude reductions seen in the Hawaii data at and below 84 km, particularly during the latter part of this data interval, are an artifact of the much lower data rates at these altitudes during this campaign at this site.

More importantly, perhaps, from the perspective of tidal coherence are the correlations between amplitude variations observed by the different radars. As noted in another paper in this special issue by *Nakamura et al.* [this issue] addressing gravity wave/tidal interactions more generally, there are many intervals during which the tidal amplitude variations are highly correlated among different sites. But these variations often do not occur at zero lag. As is clear from the amplitude variations displayed in Figure 11, this was also the case for the August 1994 interval. The dominant periods of tidal amplitude variability in each data set are ~5 to 16 days, but there is little or no correlation in time between the maximum amplitudes even for comparable instrumentation at closely-spaced sites.

In contrast to the tidal amplitude variations, tidal phase estimates are reasonably consistent among the three radars. At altitudes and times where both tidal amplitudes are sufficient for valid phase determinations, the meridional winds are in approximate phase agreement, with Hawaii lagging Christmas Island by a few hours or less above ~85 km and generally in phase with Adelaide. Below ~85 km, the phase differences between Hawaii and Christmas Island increase, but at altitudes where the amplitudes are smaller and the phase estimates less reliable. Zonal phase estimates likewise agree very well between Hawaii and Christmas Island, while Hawaii and Adelaide zonal winds are more nearly in antiphase. Phase slopes with height at Hawaii and Adelaide suggest vertical wavelengths of ~25 to 40 km during times with larger amplitudes and longer wavelengths, or more nearly evanescent behavior, at times with smaller amplitudes. Phases at Christmas Island are more variable with height (due in part to the smaller amplitudes) and imply generally longer vertical wavelengths.

The lack of temporal coherence of the diurnal tide wind variations at the three MF radars implies little or no ability to predict the tidal amplitude variability at Alcantara. Given that tidal amplitude estimates are only possible with any confidence during the two key days, these measurements provide no ability to corre-

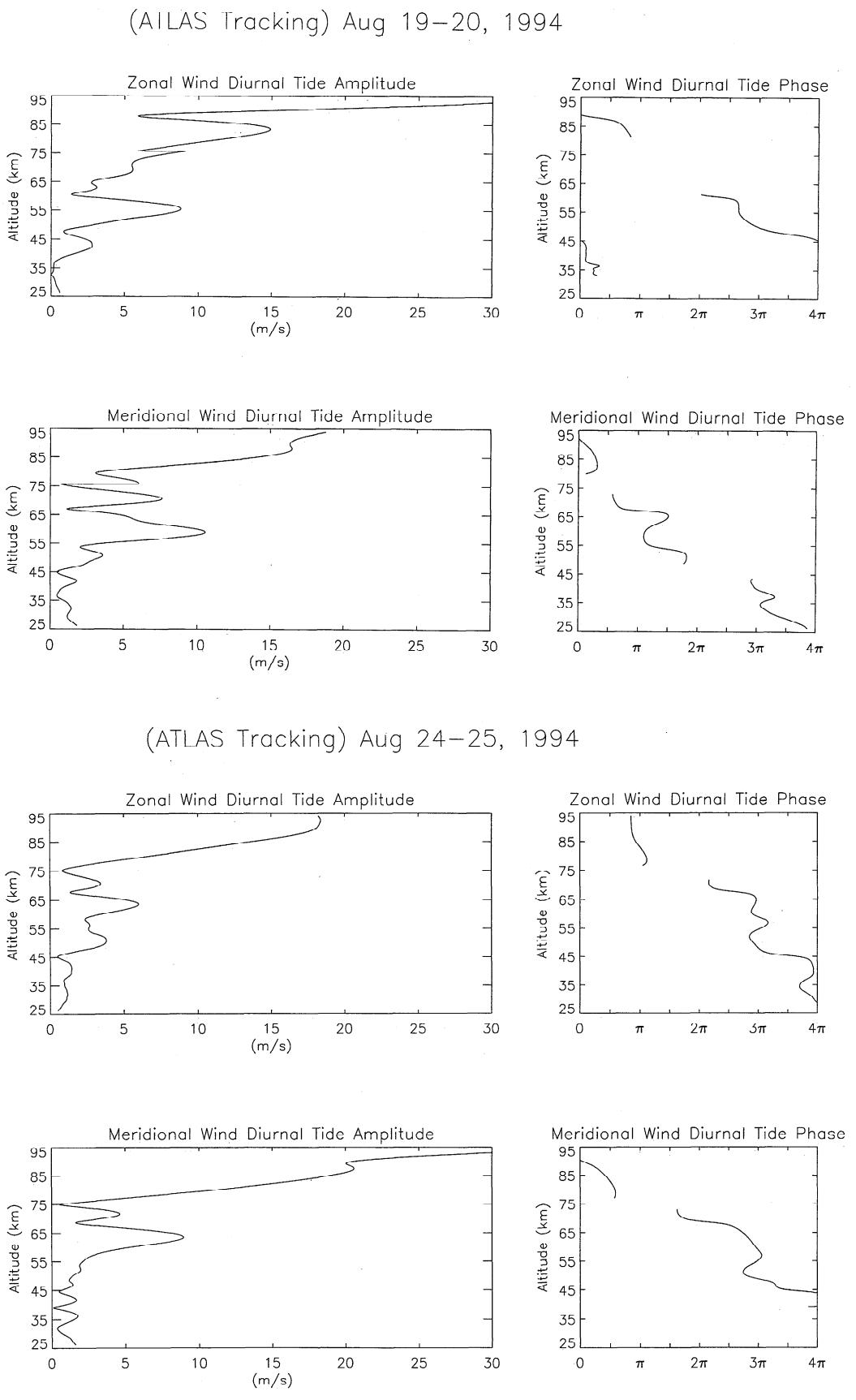

Figure 12. Diurnal tide zonal and meridional wind amplitudes and phases estimated from meteorological rocket wind profiles during the two key days of the MALTED campaign.

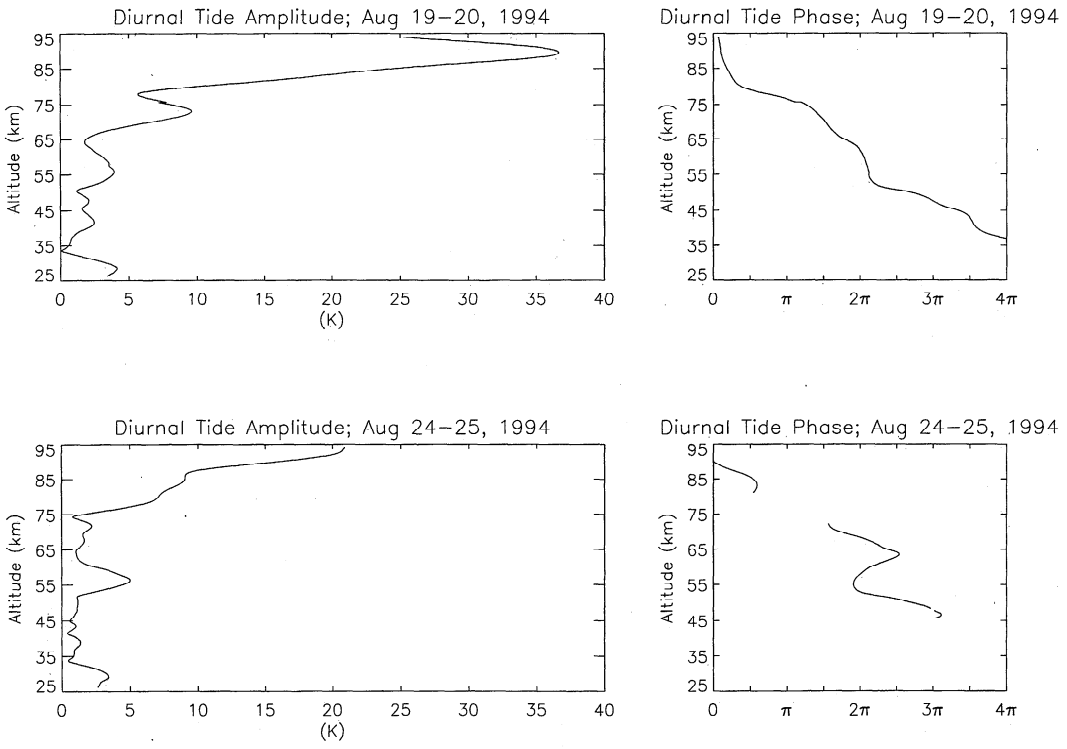

Figure 13. As in Figure 12, but for the diurnal tide temperature amplitudes and phases.

late the (possible) variability at this site with that measured by the MF radars. We can nevertheless provide estimates of the tidal wind and temperature amplitudes and phases over a considerable depth of the atmosphere, provided that the rocket measurement resolution is better than the tidal amplitudes. To examine this possibility, we display in Figures 12 and 13 the zonal and meridional winds and temperatures, as well as their estimated phases, with altitude for each key day. The variability in these estimates arises from the contributions of other wave motions to the individual wind profiles, but appears not to prevent plausible inferred tidal amplitudes and phases. Note also that fewer profiles were used in the fits above ~76 km since one payload was only tracked below this altitude.

Inferred tidal winds increase from a few meters per second in the lower stratosphere to ~20 or 30 m s^{-1} at the upper heights. Maximum tidal winds in each case occur at altitudes above 85 km, generally consistent with the MF radar measurements. Phase estimates at altitudes where amplitudes are sufficient to enable meaningful fits also exhibit general consistency, with an inferred vertical wavelength of ~25 to 30 km. Tidal temperature perturbations reveal similar variations in amplitude and phase, again with maximum amplitudes of ~20 to 40 K above 85 km and phase variations consistent with those accompanying the wind estimates. We note, however, that the greatest uncertainties in the MR wind and temperature estimates occur at the highest altitudes, thus rendering tidal amplitude estimates less reliable above ~85 km. The largest inferred temperature amplitude occurs for the first key day for which the temperature gradients in individual profiles exceeded −20 K km^{-1} at these altitudes. The second key day also exhibited superadiabatic gradients of ~−14 K km^{-1}, but yielded a smaller inferred tidal temperature amplitude throughout the altitude range.

Individual profiles and inferred tidal amplitudes imply that the diurnal tide approaches or exceeds the amplitude needed to achieve a state of convective instability above ~85 km. Implications of this apparent instability of the equatorial motion field are examined in greater detail in association with the turbulence discussion in the companion paper by *Goldberg et al.* [this issue].

4.2. Two-Day Wave Observations

Like the diurnal tide at the MF radar locations, the 2-day wave exhibits amplitude variability on planetary wave timescales, with the most obvious periodicity in the August 1994 data set ~16 days. These variations are consistent with those noted previously in the tidal amplitudes at Hawaii by *Fritts and Isler* [1994]. Unlike the diurnal tide, however, the 2-day wave amplitude variations are generally well correlated in time as displayed in Figure 14. This is especially true for the Hawaii and Christmas Island data, where zonal wind maxima occur during the first few days of the month and from about August 16 to 18 and meridional wind maxima occur a few days later in each case. Ade-

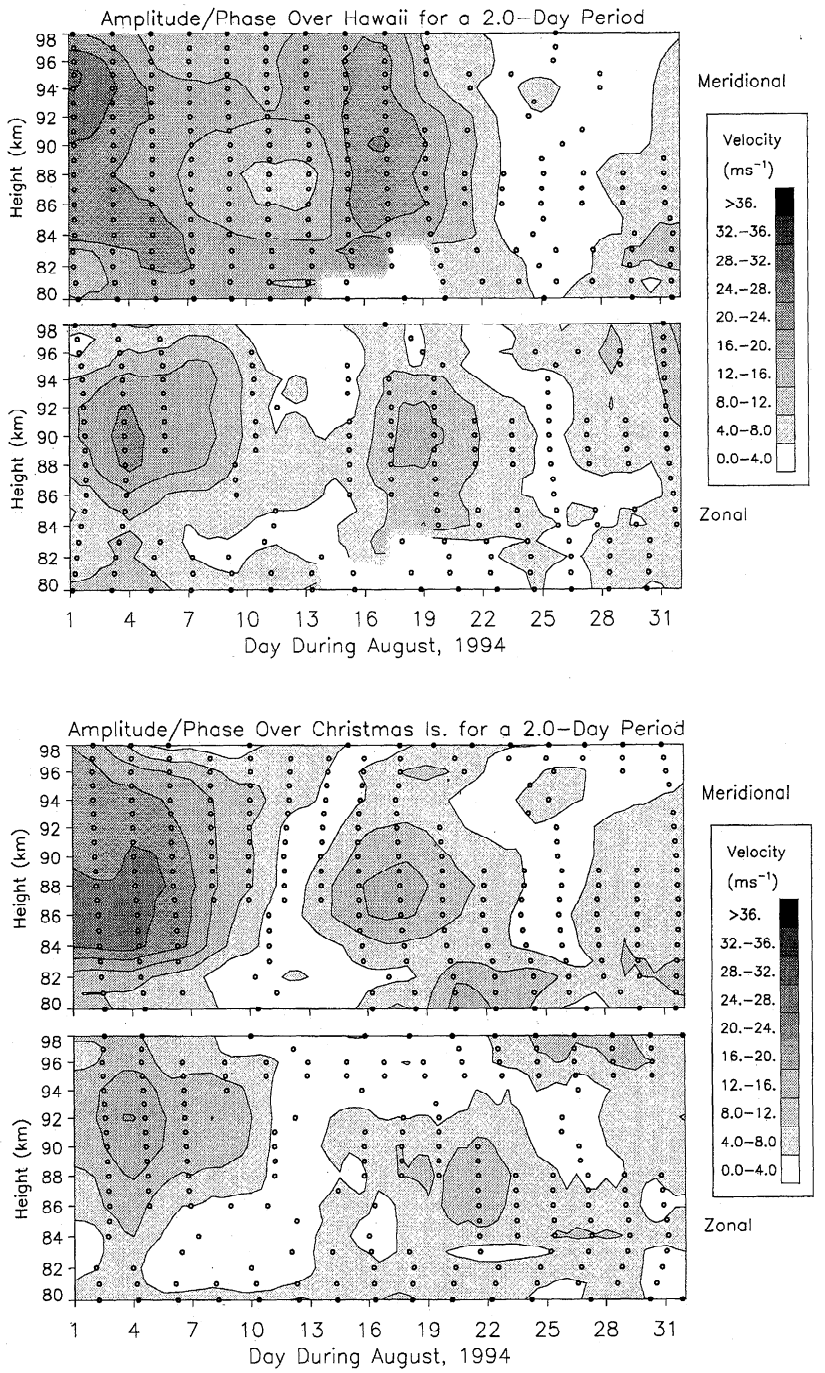

Figure 14. As in Figure 11, but for 2-day wave amplitude and phase estimates at (a) Hawaii, (b) Christmas Island, and (c) Adelaide.

laide data correlate somewhat less well, perhaps because the 2-day wave appears to be primarily a summer hemisphere event, but the second maxima of zonal and meridional winds nevertheless correlate reasonably with those at the other sites.

Times of maximum amplitude for the 2-day wave differ among the three MF radar sites, with the maximum amplitude at Hawaii during the first event leading that at Christmas Island by ~24 hours in both wind components. This phase difference decreases during the second amplitude maximum, with Hawaii leading by ~10 hours in the meridional component and with the two sites in phase in the zonal component. Indeed, the tendency throughout August 1994 is for the time of maximum in each component to experience a successive lag at Hawaii relative to Christmas Island, suggestive of different dominant periods of the observed motion at the two sites. This phase shift is much more prevalent in the zonal than in the meridional component, implying a period of nearly 48 hours at Christmas Island and in the

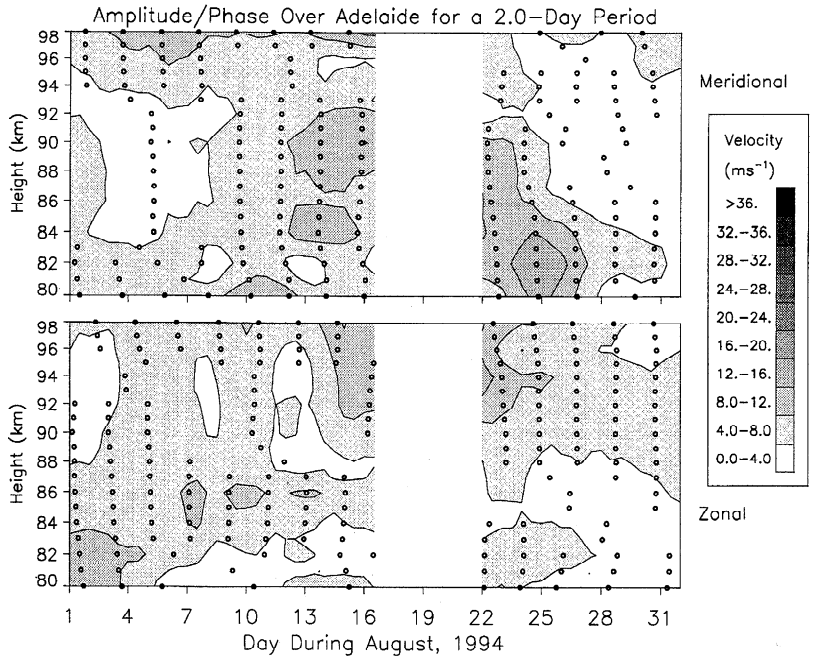

Figure 14. (continued)

meridional component at Hawaii, but nearer 50 hours in the zonal wind component. Interestingly, the relative phase shifts reverse at Adelaide, with the zonal component here exhibiting a period very near 48 hours and the meridional component displaying a period closer to 50 hours. These observations appear to confirm the mixture of modes inferred in previous studies of the northern hemisphere 2-day wave events [*Harris and Vincent,* 1993; *Fritts and Isler,* 1994; *Randel,* 1994; *Meek et al.,* 1996].

5. Small-Scale Motions

We turn now to an examination of the smaller-scale motions in the equatorial lower and middle atmosphere observed by MR and the Jicamarca MST radar during the MALTED campaign. For this purpose, we wish to use only those data for which the amplitudes are much larger than the measurement uncertainties. Perturbation winds for each rocket wind profile were obtained by subtracting the appropriate mean wind profile for the rocket campaign. The resulting zonal (top) and meridional (bottom) perturbation winds obtained using the Atlas (solid lines) and NASA (dashed lines) tracking radars and the filtering scheme discussed in section 2 are shown in Figure 15 at altitudes from ~26 to 60 km.

In general, the motion field at smaller scales and equatorial latitudes includes gravity waves, equatorial waves, inertial and other instabilities, and two- and three-dimensional turbulent structures. Gravity waves at these latitudes span intrinsic frequencies from the inertial to the buoyancy frequency and thus contribute at a wide range of horizontal and vertical scales. Equatorial wave motions include Kelvin and mixed Rossby-gravity waves having lower zonal wavenumbers, faster motions having larger vertical scales, and smaller-scale, slower motions having smaller vertical scales and contributing primarily at lower altitudes. Inertial instability structures are also observed at equatorial latitudes, primarily in the winter hemisphere, and arise from unstable mean flows due to cross-equatorial advection of stable horizontal shears in the summer hemisphere. Dynamical and convective instabilities play important roles at smaller scales in stabilizing wave and mean shears and in generating turbulent structures in two and three dimensions. Of these motions, however, gravity waves appear to account for the majority of the spectral variance at higher frequencies.

5.1 Gravity Waves

The wind profiles displayed in Figure 15 exhibit fluctuations increasing in amplitude and vertical wavelength with increasing altitude. Dominant scales are typically ~1 to 3 km below 30 km and increase to ~5 to 10 km at greater heights. To some extent, smaller scales at greater altitudes are suppressed by the increased spatial smoothing with altitude of the MR data. Nevertheless, both characteristics scales and amplitudes experience increases with altitude that are consistent with previous radar studies throughout the atmosphere. Also seen in these profiles, particularly those spaced more closely in time, are wavelike features which are coherent, but often with some sense of phase progression, among successive profiles. This coherence was noted previously in the discussion of the complete rocket wind profiles, but the perturbation profiles enable us to examine these features apart from mean wind structures. In most instances, such wind fluctuations and their varying am-

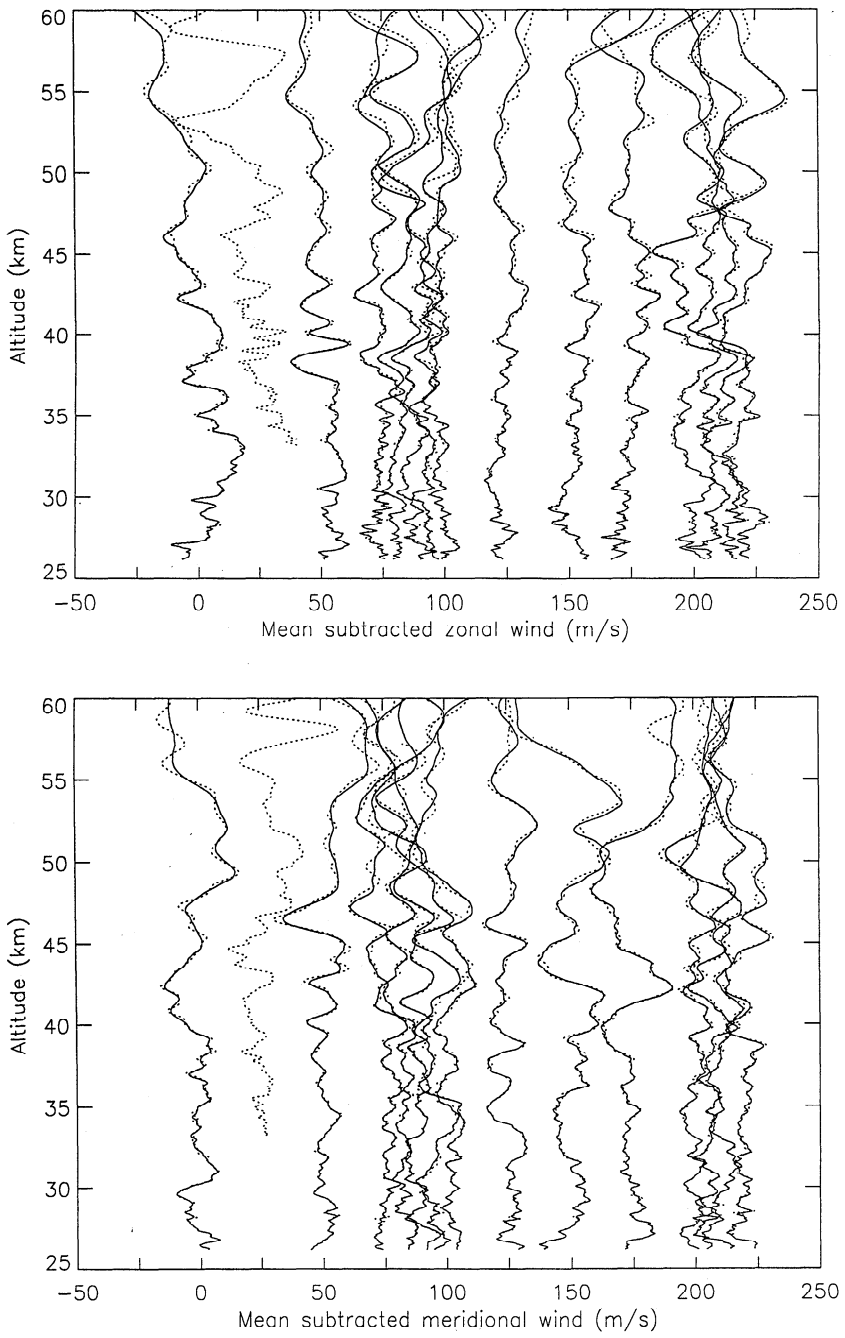

Figure 15. Perturbation (top) zonal and (bottom) meridional winds obtained by meteorological rockets with Atlas (solid) and NASA (dashed) tracking systems after subtraction of the campaign mean winds. These data are displayed only to 60 km to focus on those altitudes at which the perturbation wind estimates agree well between the two tracking systems. Successive profiles are displaced by 25 m s^{-1} per 24-hour interval.

plitudes and vertical scales with altitude have been interpreted as manifestations of internal gravity waves [*Smith et al.*, 1987; *Fritts et al.*, 1988; *Tsuda et al.*, 1989], and we make the same assumption here.

Importantly from our measurement perspective, there are virtually no differences between the perturbation winds inferred by the Atlas and NASA tracking systems below ~40 km. The differences do increase above 40 km, but in most cases remain significantly smaller than the perturbation winds themselves. Given the agreement between the winds inferred with each tracking radar up to 60 km, we can use either data set to compare the zonal and meridional wind fluctuations below this altitude. Thus, we display together in Figure 16 the zonal (solid) and meridional (dashed) perturbation winds obtained using the Atlas tracking system for all MRs (top) and for those five comprising the first key day measurement series (bottom).

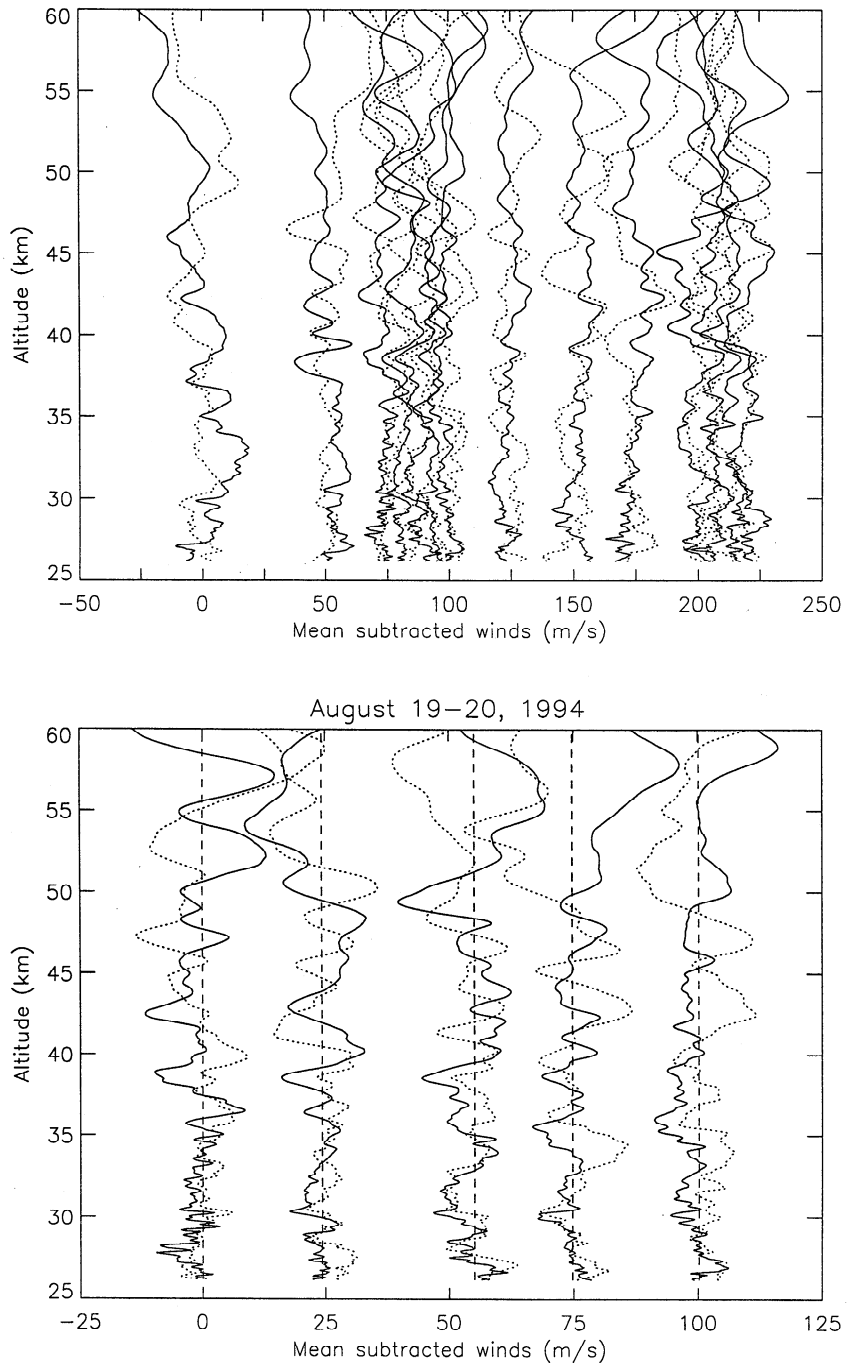

Figure 16. As in Figure 15, but showing the (solid) zonal and (dashed) meridional perturbations winds from the Atlas trackings for all meteorological rockets (top) and for the first key day (bottom). Successive profiles in the lower panel are displaced 100 m s^{-1} per 24-hour interval.

Coherent structures are seen in Figures 15 and 16 at a number of heights. Those noted earlier near 40 km in the total wind profiles during the two key days remain the most obvious. In each case, these are motions having amplitudes of ~15 m s^{-1} and vertical wavelengths of ~3 to 5 km which are very persistent in time. In both cases, in fact, there is a suggestion of the same motion in the previous daily wind profile or two. These features suggest low-frequency gravity waves with very slow vertical phase progression, due either to very low intrinsic frequencies or to eastward propagation of higher-frequency motions in the westward mean flow at these altitudes.

But there are also persistent or coherent propagating features at a number of other heights in the perturbation wind profiles suggestive of gravity wave motions at various scales. Examples include the ~2 to 3 km wavelength just below 40 km and between the two key days, the ~1/2 to 1 km features during the first key day from ~28 to 31 km, and structures at simi-

lar scales below 28 km and between ~34 and 37 km during the second key day. Unfortunately, small-scale and/or higher-frequency wave structures are difficult to correlate unambiguously over large time intervals because of their large vertical phase and group velocities compared to the resolution capabilities of all but the closely-spaced rocket profiles. To be discerned clearly, a wave must propagate significantly less than one wavelength between observations. This imposes the condition, $c_z \Delta t << \lambda_z$, where c_z is the vertical phase velocity, Δt is the interval between soundings, and λ_z is the vertical wavelength. Since $c_z \simeq \lambda_z / T_i$, where T_i is the intrinsic period of the wave motion, this requires that $\Delta t << T_i$. Thus, the only motions that satisfy this condition are those occurring very near the inertial frequency, for the daily rocket spacings at least. The majority of gravity wave frequencies (and likely energy densities) do not satisfy this condition and thus would appear to have no coherence between profiles even if they were well-defined, large-amplitude wave motions.

An alternative approach to identifying distinct wave motions in individual rocket or balloon soundings is to seek correlated zonal and meridional winds and temperatures with scales and amplitudes satisfying the dispersion relation for a particular intrinsic frequency and direction of propagation. This approach has been used by *Hirota and Niki* [1986], and *Eckermann et al.* [1995] to determine the statistical properties of the gravity wave field with various data sets. It is a powerful technique, in general, and also permits estimates of momentum flux magnitudes and directions for the dominant components of the motion field. Its applicability to our rocket soundings is limited, however, by our lack of confidence in the small-scale temperature determinations. We may, nevertheless, infer all gravity wave parameters, except for an ambiguity in the direction of propagation, from the wind profiles alone for sufficiently monochromatic events. But in most instances, superposition of several wave motions having different scales and intrinsic properties introduces uncertainties to this process. Superposition of two high-frequency motions with comparable vertical scales may likewise be confused with a wave influenced more strongly by rotation, as argued by *Eckermann et al.* [1995].

At southern latitudes, $f = 2\Omega \sin\phi < 0$ and anticyclonic (counter-clockwise) rotation of an IGW horizontal wind vector with increasing altitude is indicative of a downward phase velocity and an upward group velocity (assuming the wave not to be Doppler shifted to an oppositely signed horizontal phase velocity). Cyclonic rotation with height implies upward phase propagation and a downward group velocity, while correlated or anticorrelated wind structures signify relatively higher-frequency motions having a plane of propagation in the direction of maximum horizontal wind variation.

Referring again to Figure 16, particularly the five key-day profiles in the lower panel, we see good examples of anti-cyclonic rotation with height at ~3- to 5-km vertical wavelengths below ~35 km in the third pair of profiles and in the last two soundings up to ~40 km. The latter structures, especially, are also well correlated in time, further supporting their interpretation as low-frequency gravity waves. At other times, the larger-scale, more coherent structures appear to have a cyclonic rotation with height, implying a source of these motions at greater altitudes. The most conspicuous examples of this behavior occur at ~5-km vertical wavelengths between ~35 to 45 km in the first two pairs of profiles.

There are also many examples of higher-frequency events in the profiles displayed in Figure 16. A few of the more obvious in the upper panel include the correlated winds (gravity waves propagating toward the northeast or southwest) at ~1- to 2-km scales at altitudes near 40 km in the second and ninth profile pairs and the anticorrelated winds (waves propagating toward the northwest or southeast) at ~1/2- to 1-km scales near 30 km and below in the ninth profile pair. Examples during the first key day (lower panel) include the anticorrelated winds at ~1- to 2-km scales and between ~40 and 50 km in the first and third pairs of profiles and the correlated winds at small vertical scales below ~33 km in the first profiles of this key day.

The rocket wind measurements discussed here provide valuable information on the spatial and temporal scales of the gravity waves present in the equatorial middle atmosphere, particularly at altitudes at which radar and balloon measurements are not possible. Without an ability to assess the intrinsic properties and directionality of the gravity waves present in the rocket wind profiles, however, it is difficult to quantify the roles of those gravity waves accounting for the observed wind fluctuations. To provide this quantitative ability in association with the MALTED rocket campaign, we have employed the Jicamarca MST radar using a beam configuration designed for momentum flux measurements. The results of these measurements are discussed below.

5.2 Gravity Wave Momentum Fluxes

The Jicamarca MST radar was used for the MALTED campaign in a four-beam configuration originally implemented by *Fritts et al.* [1992] and *Hitchman et al.* [1992] specifically for momentum flux measurements. The details of the radar measurements and of the data collection and analysis procedures are described by *Riggin et al.* [this issue (b)] in this issue. Here we provide only a brief summary of the measurement capabilities and analysis techniques.

The Jicamarca MST radar is a 50-MHz system having a phased dipole array and a peak power of approximately 1 MW. For the MALTED campaign, the antenna was divided into four quadrants, phased to provide beams in the north, south, east, and west directions at zenith angles of 2.5°. The small zenith angle was chosen to minimize grating lobes while achieving a zenith angle as large as possible compared to the 0.6°

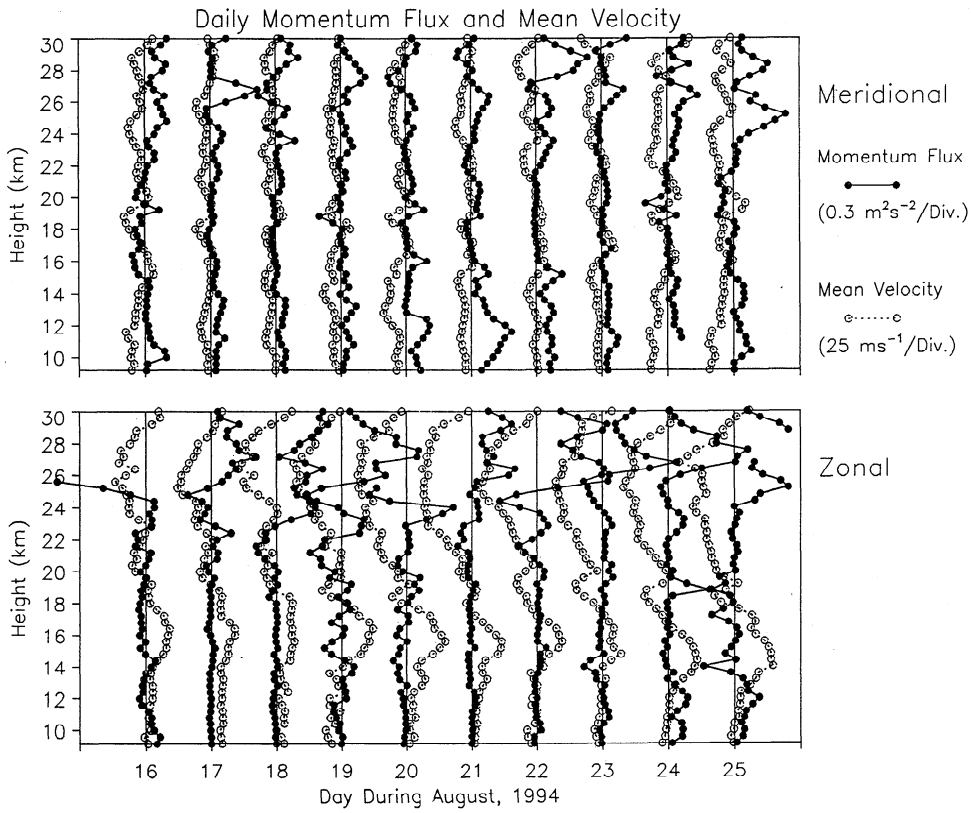

Figure 17. Daily mean winds (open circles) and momentum fluxes (solid circles) in the (bottom) zonal and (top) meridional directions in the troposphere and lower stratosphere measured using the Jicamarca MST radar from August 16 to 25, 1994.

two-way, half-power beamwidth in the plane of beam steering.

Data were collected using a 20-baud complementary code, a 2.67 μs or 400 m baud length, full decoding above 19.2 km, and a scheme for partial decoding at lower altitudes following *Spano et al.* [1991] enabling radial velocity estimates down to 9.2 km. Useful data were thus obtained from 9.2 to 32 km due to neutral atmosphere refractive index fluctuations and from ~60 to 94 km due to electron density gradients at small scales of motion. At greater altitudes, data were limited by the lower edge of the equatorial electrojet, which normally has a much larger scattering cross-section than mesospheric ionization above 95 km.

Velocity estimates in the mesosphere were obtained using 64-point FFT's which were then incoherently averaged, yielding a time resolution of one minute. In the troposphere and lower stratosphere, more spectral resolution was needed to minimize contamination by fading clutter at zero Doppler from the surrounding mountains. Thus velocity estimates were obtained with 256-point FFT's and two-minute incoherent averaging at these altitudes. The resulting data were then thresholded on the basis of S/N, spectral width, and other criteria. Northward and eastward velocities were derived from the radial components following the procedure described by *Hitchman et al.* [1992]. Additional averaging of the velocities was performed to estimate the motions associated with longer time scales. When averaging the data, outliers were removed by detrending the data in each bin and applying Chauvenet's criterion, which is more tolerant of outliers as the number of points in the distribution increases [*Young,* 1962]. Momentum fluxes were estimated using the method described by *Riggin et al.* [this issue (b)]. Essentially, this is an extension of the technique introduced by *Vincent and Reid* [1983] which takes advantage of additional confidence in the vertical velocities when multiple beams are used for its estimation.

Daily-averaged momentum flux profiles in the zonal and meridional directions are shown together with the mean winds in each direction in the troposphere and lower stratosphere in Figure 17 and in the mesosphere in Figure 18 throughout the MALTED campaign. Daily-averaged momentum fluxes in the troposphere tended to be small. Typical magnitudes are ~0.1 m^2 s^{-2} or less in the meridional direction and even smaller in the zonal direction. Mean meridional winds and momentum fluxes are often approximately anti-correlated in height, while zonal momentum fluxes are only weakly negative at the altitudes of maximum eastward mean motion in the lower phase of the QBO. These results suggest a gravity wave spectrum that is either approximately isotropic in the zonal direction or has primarily

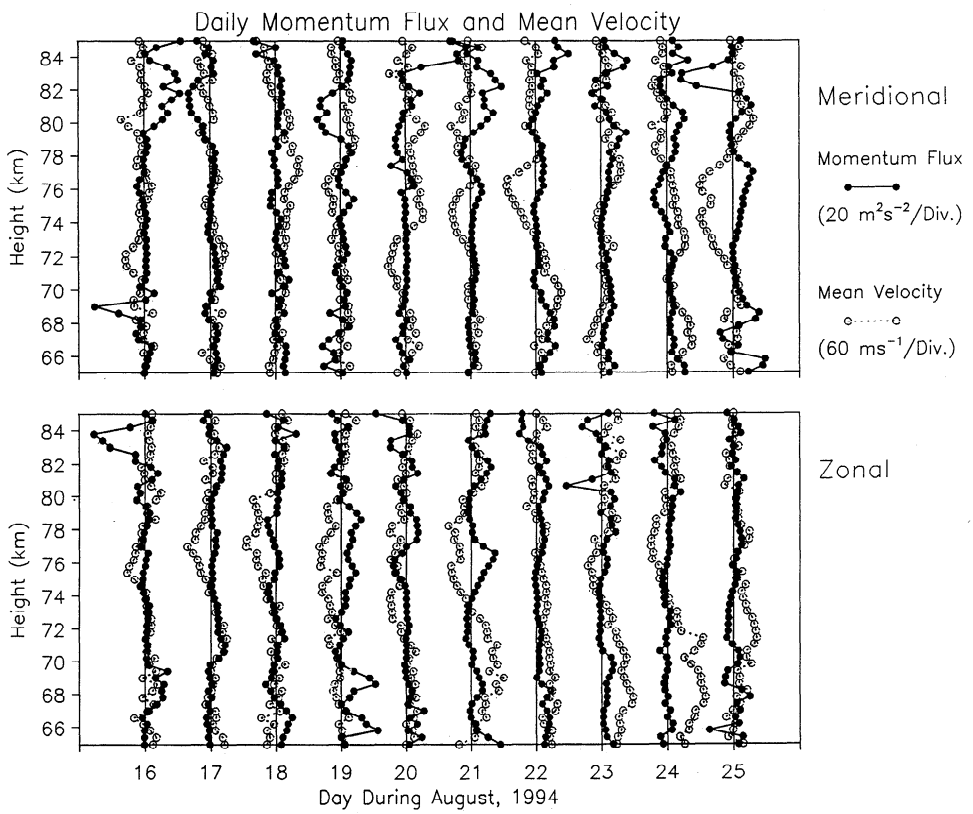

Figure 18. As in Figure 17, but in the mesosphere.

meridional propagation at these altitudes, perhaps due to filtering of the spectrum by tropospheric wind shears at lower levels. But this is just what would be expected if a predominant source of wave activity was orography, with westward surface flow below eastward motions at greater altitudes.

In the lower stratosphere, the relative magnitudes of the zonal and meridional momentum fluxes have reversed. As in the troposphere, mean meridional fluxes and winds are largely anti-correlated, with typical momentum flux magnitudes of ~ 0.1 m^2 s^{-2}. Also noted above $\sim$24 km altitude is an increasing tendency for a positive correlation between the momentum flux and the vertical shear of the horizontal motion in both zonal and meridional directions.

As in the troposphere, these wind and momentum flux correlations have important implications for the gravity wave spectrum and its propagation and isotropy (or lack of) at greater altitudes. The mean winds and momentum fluxes displayed in Figures 17 and 18 suggest an explanation along the following lines. Above the active source regions for gravity waves, typically orography, convection, and wind shear within the troposphere or near the tropopause, gravity wave spectral characteristics are governed less by source characteristics and isotropy and increasingly by interactions within the wave spectrum and with the mean winds through which the waves propagate. As noted in many previous efforts, a spectrum of gravity waves propagating through a region with a mean wind shear will experience a removal or suppression of those components approaching critical levels due to the mean shear. This reduces the momentum flux in the direction of the wind shear and enhances the net flux in the opposite direction.

Such filtering also has a cumulative effect, removing or suppressing an increasing fraction of the wave spectrum and increasing the oppositely signed momentum flux with altitude. Since gravity wave amplitudes (and momentum fluxes) in general increase with increasing altitude, this anti-correlation of shears and momentum flux tendencies will only cease when the remaining gravity waves in the spectrum encounter an opposite wind shear. The result is a positive correlation of the wind shear and momentum flux in altitude. This simple process underlies the large majority of gravity wave interactions with mean and lower-frequency structures and is the basis for both the discrete and spectral parameterizations of such interactions employed in a variety of models [*Holton,* 1982; *Garcia and Solomon,* 1985; *Fritts and Vincent,* 1987; *Forbes et al.,* 1991; *Fritts and Lu,* 1993; *Lu and Fritts,* 1993; *Eckermann and Marks,* 1996].

Examples of the correlations described above can be seen in virtually all of the profiles displayed in Figures 17 and 18. They are especially apparent in all the meridional profiles and in the zonal profiles on August 17, 18, and 22 to 24 in the stratosphere and at larger vertical scales in the mesosphere. As a result, we con-

clude that such interactions play a fundamental role in modulating the gravity wave dynamics and transports of momentum throughout the middle atmosphere.

5.3. Instability of Gravity Wave and Tidal Motions

We now return to the topic of gravity wave and tidal instability implied by the MR and sounding rocket measurements during the MALTED campaign. While the filtering and vertical smoothing applied to the MR data effectively degrade the height resolution and remove the smaller vertical scales increasingly with altitude, we can nevertheless be confident of the wind (and shear) estimates where the Atlas and NASA data sets agree well.

At lower altitudes, we see that wind shears due to mean and low-frequency motions are often comparable to or exceed 50 m s^{-1} km^{-1} in each component of the velocity field. The maximum component shears decrease with altitude for reasons discussed above, but remain ~20 to 30 m s^{-1} km^{-1} to above 60 km. These shears are quite large, imply local Richardson numbers $Ri = N^2/(u_z^2 + v_z^2) < 1/4$, and are thus a necessary, though not sufficient, condition for instability even without temperature perturbations induced by the wave motions [*Miles,* 1961; *Howard,* 1961].

Such shears at small vertical scales are suggestive of very low frequency gravity wave motions, in which large shears may occur at wave amplitudes below that necessary for convective instability of the motion field [*Dunkerton,* 1984; *Fritts and Rastogi,* 1985]. Persistence of the small-scale flow features and the quadrature correlations between wind components on occasion at lower altitudes provide additional evidence of the low-frequency character of the motion field (see Figures 15 and 16). Higher-frequency motions, in contrast, would achieve a state of convective instability at wave shears $u_z, v_z \sim N(z)$, thus preventing the attainment of shears of the magnitudes observed [*Fritts,* 1984; *Andreassen et al.,* 1994].

These low-frequency motions are nevertheless likely to be experiencing instability and amplitude constraints due to dynamical instability of the motion field with or without mean shears [*Fritts and Yuan,* 1989; *Yuan and Fritts,* 1989; *LeLong and Dunkerton,* 1996; *Dunkerton,* 1996]. At these very low wave frequencies and small vertical scales, however, the vertical fluxes of wave energy and the associated levels of turbulence are necessarily very much smaller than where wave scales, amplitudes, and frequencies are larger.

At greater altitudes, the MR temperature profiles exhibit clear indications of convective instability within the superposed wave field, provided that the MR measurement and analysis techniques are sufficiently constrained by our narrower choice of a smoothing filter for the present study. Similar arguments also apply to the tidal estimates, which suggest convective instability of the tidal structures at greater altitudes during the first key day. Assuming a mean temperature gradient of −2 K km^{-1} and a vertical wavelength of 25 km, the temperature amplitude required for convective instability is then only ~30 K and is exceeded above 85 km. Indeed, this inference of tidal instability appears to be corroborated to some extent by the turbulence measurements by *Goldberg et al.* [this issue] which reveal a region of turbulence extending from ~85 to 90 km at the time of the inferred maximum (negative) tidal gradients. The resulting tidal amplitudes in the thermal field, while approaching or exceeding those necessary for convective instability in an environment with a negative mean gradient, particularly on the first key day, are suggestive of tidal instability only at altitudes at which the MR data yield increasingly uncertain tidal amplitude estimates. Thus, a definitive determination of whether the diurnal tide is convectively unstable in the equatorial mesosphere must await a more complete set of correlative measurements able to define both the tidal structures and the gravity wave motions with which they interact and superpose.

6. Summary and Conclusions

We have presented an analysis of wind and temperature data collected by rockets at Alcantara, Brazil, by MF and MST radars at Hawaii, Christmas Island, Adelaide, and Jicamarca, and by HRDI onboard UARS during the CADRE/MALTED campaign conducted in August 1994. The objectives of the campaign were to define the mean structure and low-frequency variability with altitude, to examine the tidal variability at planetary wave periods, and to evaluate the contributions of the various wave motions to instability processes within the equatorial middle atmosphere.

A combination of radar, rocket, and HRDI data contributed to definition of the zonal mean structure at equatorial (and in the case of HRDI, nearly global) latitudes from ~10 to 110 km. These measurements revealed a QBO in the lower stratosphere having phases and amplitudes consistent with previous data, approximate nulls in the SAO responses near the stratopause and mesopause due to the occurrence of the measurements near a phase transition in the second cycle of this oscillation, a westward jet at ~95 to 100 km, and an eastward jet at ~110 km and above. Good agreement between the HRDI and MF radar winds at MLT altitudes was also noted for the radars at Hawaii and Adelaide, suggesting that these sites provided reasonable approximations to the mean zonal motions at those latitudes.

Noted in the MF radar data was considerable variability at planetary wave periods. A significant oscillation primarily in the zonal velocity was noted at Hawaii and Christmas Island at a period near 7 days. Shorter-period motions were also noted, again primarily in the zonal component, with periods near 4 and 2.7 days at Hawaii. The dominant motion in the meridional component, by comparison, was the 2-day wave, with a maxi-

mum response at Christmas Island and occurring near the beginning of the measurement campaign.

Tidal amplitudes measured by the three MF radars were found to exhibit significant variations on planetary wave periods but to be poorly correlated, in general, among these three sites. Dominant periods were $\sim$ 8 and 16 days, as noted in previous studies. Two-day wave amplitude variations, in contrast, agreed reasonably well between the two sites (Hawaii and Christmas Island) expected to exhibit significant responses to the northern hemisphere summer event and displayed the same periodicities as the diurnal tide. Meteorological rocket estimates of tidal structures yielded amplitudes increasing from a few m s^{-1} and K in the lower stratosphere to $\sim$20 m s^{-1} and 20 to 40 K in the upper mesosphere. The large inferred amplitudes in the thermal structure suggest that the diurnal tide achieves a state of convective instability on occasion at equatorial latitudes and MLT altitudes.

Rocket measurements at smaller vertical scales revealed considerable coherence between successive rocket wind measurements and a clear tendency for a quadrature relation between the two wind components, suggestive of inertia-gravity wave motions having significant vertical shears. MST radar measurements of gravity wave momentum flux showed these fluxes and the mean winds to be generally anticorrelated at lower levels, with a tendency for an increasing (positive) correlation between wind shear and the momentum flux with increasing altitude. Because of the significant fluxes associated with inertia-gravity waves at equatorial latitudes and their large vertical shears, we expect these small-scale (and low-frequency) motions to play a major role in the dynamics of the equatorial atmosphere.

Acknowledgments. This research was supported by the National Aeronautics and Space Administration under grants NAG5-5014, NAG1-1440, and NAG5-2786 and by the National Science Foundation under grants ATM91-18899 and ATM94-14177.

References

Andreassen, Ø., C.-E. Wasberg, D. C. Fritts, and J. R. Isler, Gravity wave breaking in two and three dimensions, 1., Model description and comparison of two-dimensional evolutions, *J. Geophys. Res., 99,* 8095–8108, 1994.

Delisi, D. P., and T. J. Dunkerton, Seasonal variation of the semiannual oscillation, *J. Atmos. Sci., 45,* 2772–2787, 1988.

Dunkerton, T. J., Theory of the mesopause semiannual oscillation, *J. Atmos. Sci., 39,* 2681–2690, 1982.

Dunkerton, T. J., Inertio-gravity waves in the stratosphere, *J. Atmos. Sci., 41,* 3396–3404, 1984.

Dunkerton, T. J., Shear instability of internal gravity waves, *J. Atmos. Sci., 53,* in press, 1997.

Dunkerton, T. J., Role of gravity waves in the quasi-biennial oscillation, *J. Geophys. Res.,* this issue, 1997.

Eckermann, S. D., On the observed morphology of gravity-wave and equatorial-wave variance in the stratosphere, *J. Atmos. Terr. Phys., 57,* 105–134, 1995.

Eckermann, S. D., I. Hirota, and W. K. Hocking, Gravity wave and equatorial wave morphology of the stratosphere derived from long-term rocket soundings, *Q. J. R. Meteorol. Soc., 121,* 149–186, 1995.

Eckermann, S. D., and C. J. Marks, An idealized ray model of gravity wave-tidal interactions, *J. Geophys. Res., 101,* 21,195–21,212, 1996.

Forbes, J. M., J. Gu, and S. Miyahara, On the interactions between gravity waves and the propagating diurnal tide, *Planet. Space Sci., 39,* 1249–1257, 1991.

Fritts, D. C., Gravity wave saturation in the middle atmosphere: A review of theory and observations, *Rev. Geophys., 22,* 275–308, 1984.

Fritts, D. C., and P. K. Rastogi, Convective and dynamical instabilities due to gravity wave motions in the lower and middle atmosphere: Theory and observations, *Radio Sci., 20,* 1247–1277, 1985.

Fritts, D. C., and R. A. Vincent, Mesospheric momentum flux studies at Adelaide, Australia: Observations and a gravity wave/tidal interaction model, *J. Atmos. Sci., 44,* 605–619, 1987.

Fritts, D. C., T. Tsuda, T. Sato, S. Fukao, and S. Kato, Observational evidence of a saturated gravity wave spectrum in the troposphere and lower stratosphere, *J. Atmos. Sci., 45,* 1741–1759, 1988.

Fritts, D. C., and L. Yuan, An analysis of gravity wave ducting in the atmosphere: Eckarts resonances in thermal and Doppler ducts, *J. Geophys. Res., 94,* 18,455–18,466, 1989.

Fritts, D. C., L. Yuan, M. H. Hitchman, L. Coy, E. Kudeki, and R. F. Woodman, Dynamics of the equatorial mesosphere observed using the Jicamarca MST radar during June and August 1987, *J. Atmos. Sci., 49,* 2353–2371, 1992.

Fritts, D. C., and W. Lu, Spectral estimates of gravity wave energy and momentum fluxes, II: Parameterization of wave forcing and variability, *J. Atmos. Sci., 50,* 3695–3713 1993.

Fritts, D. C., and J. R. Isler, Mean motions and tidal and two-day structure and variability in the mesosphere and lower thermosphere over Hawaii, *J. Atmos. Sci., 51,* 2145–2164, 1994.

Fritts, D. C., J. F. Garten, and Ø. Andreassen, Wave breaking and transition to turbulence in stratified shear flows, *J. Atmos. Sci., 53,* 1057–1085, 1996.

Fritts, D. C., An overview of the CADRE measurement campaigns and scientific objectives, *J. Geophys. Res.,* this issue.

Garcia, R. R., and S. Solomon, 1985: The effect of breaking gravity waves on the dynamical and chemical composition of the mesosphere and lower thermosphere, *J. Geophys. Res., 90,* 3850–3868.

Garcia, R. R., T. J. Dunkerton, R. S. Lieberman, and R. A. Vincent, Climatology of the semiannual oscillation of the tropical middle atmosphere, *J. Geophys. Res.,* this issue.

Goldberg, R. A., G. Lehmacher, F. J. Schmidlin, D. C. Fritts, J. D. Mitchell, C. L. Croskey, M. Friedrich, and W. E. Swartz, Equatorial dynamics observed by rocket, radar, and satellite during the CADRE/MALTED Campaign: 1. Programmatics and small scale fluctuations, *J. Geophys. Res.,* this issue.

Hamilton, K., Rocketsonde observations of the mesospheric semiannual oscillation at Kwajalein, *Atmos. Ocean., 20,* 281–286, 1982.

Harris, T. J., and R. A. Vincent, The quasi-two-day wave observed in the equatorial middle atmosphere, *J. Geophys. Res., 98,* 10481–10490, 1993.

Hays, P. B., V. J. Abreu, M. E. Dobbs, D. A. Gell, H. J. Grassl, and W. R. Skinner, The High Resolution Doppler Imager on the Upper Atmosphere Research Satellite, *J. Geophys. Res., 98,* 10,713–10,723, 1993.

Hirota, I., Equatorial waves in the upper stratosphere and mesosphere in relation to the semiannual oscillation of the zonal mean wind, *J. Atmos. Sci., 35,* 714–722, 1978.

Hirota, I., and T. Niki, A statistical study of inertia-gravity waves in the middle atmosphere, *J. Meteorol. Soc. Jpn., 63,* 995–999, 1986.

Hitchman, M. H., and C. B. Leovy, Evolution of the zonal mean state in the equatorial middle atmosphere during October 1978–May 1979, *J. Atmos. Sci., 43,* 3159–3176, 1986.

Hitchman, M. H., K. W. Bywaters, D. C. Fritts, L. Coy, and E. Kudeki, Mean winds and momentum fluxes over Jicamarca, Peru during June and August 1987, *J. Atmos. Sci., 49,* 2372–2383, 1992.

Hitchman, M. H., J. M. Kugi, G. A. Postel, C.-Y. Yao, V. Lynn Harvey, E. Kudeki, C. Fawcett, D. C. Fritts, D. Riggin, and D. Ortland, Mean winds in the tropical stratosphere and mesosphere during January 1993, March 1994, and August 1994, *J. Geophys. Res.,* this issue.

Holton, J. R., The role of gravity wave-induced drag and diffusion in the momentum budget of the mesosphere, *J. Atmos. Sci., 39,* 791–799, 1982.

Holton, J. R., and H.-C. Tan, The influence of the equatorial quasi-biennial oscillation on the global circulation at 50 mb, *J. Atmos. Sci., 37,* 2200–2208, 1980.

Holton, J. R., and H.-C. Tan, The quasi-biennial oscillation in the Northern Hemisphere lower stratosphere, *J. Meteorol. Soc. Jpn., 60,* 140–148, 1982.

Howard, L. N., Note on a paper by John W. Miles, *J. Fluid Mech., 10,* 509–512, 1961.

LeLong, M.-P., and T. J. Dunkerton, Shear and convective instabilities in breaking inertia-gravity waves, *J. Atmos. Sci., 53,* submitted.

Lieberman, R. S., and P. B. Hays, An estimate of the momentum deposition in the lower thermosphere by the diurnal tide, *J. Atmos. Sci., 51,* 3094–3105 1994.

Lieberman, R. S., and D. Riggin, HRDI observations of Kelvin waves in the equatorial mesosphere and lower thermosphere, *J. Geophys. Res.,* this issue.

Lu, W., and D. C. Fritts, Spectral estimates of gravity wave energy and momentum fluxes, III: Gravity wave-tidal interactions, *J. Atmos. Sci., 50,* 3714–3727, 1994.

McLandress, C., G. G. Shepherd, B. H. Solheim, M. D. Burrage, P. B. Hays, and W. R. Skinner, Combined mesosphere/thermosphere winds using WINDII and HRDI data from the Upper Atmosphere Research Satellite, *J. Geophys. Res., 101,* 10,441–10,453, 1996.

Meek, C. E., et al., Global study of northern hemisphere quasi-2-day wave events in recent summers near 90 km altitude, *J. Atmos. Terr. Phys., 58,* 1401–1411, 1996.

Miles, J. W., On the stability of heterogeneous shear flows, *J. Fluid Mech., 10,* 496–508, 1961.

T. Nakamura, D. C. Fritts, J. R. Isler, T. Tsuda, and R. A. Vincent, 1997: Short-period fluctuations of the diurnal tide observed with low-latitude MF and meteor radars during CADRE: Evidence for gravity wave/tidal interactions, *J. Geophys. Res.,* this issue.

OŚullivan, D. J., and M. L. Salby, Coupling of the quasi-biennial oscillation and the extratropical circulation in the stratosphere through planetary wave transports, *J. Atmos. Sci., 46,* 650–573, 1989.

Plumb, R. A., and R. C. Bell, A model of the quasi-biennial oscillation on an equatorial beta-plane, *Q. J. R. Meteorol. Soc., 108,* 335-352, 1982.

Plumb, R. A., and A. D. McEwan, The instability of a forced standing wave in a viscous stratified fluid: A laboratory analog of the quasi-biennial oscillation, *J. Atmos. Sci., 35,* 1827–1839, 1978.

Randel, W. J., Observations of the 2-Day wave in NMC stratospheric analyses, *J. Atmos. Sci., 51,* 306–313, 1994.

Riggin, D., D. C. Fritts, C. W. Fawcet, E. Kudeki, and M. H. Hitchman, Radar observations of gravity waves over Jicamarca, Peru during the CADRE campaign, *J. Geophys. Res.,* this issue (a).

Riggin, D., D. C. Fritts, T. Tsuda, T. Nakamura, and R. A. Vincent, Radar observations of a 3-day Kelvin wave in the equatorial mesosphere, *J. Geophys. Res.,* this issue (b).

Sato, K., and T. J. Dunkerton, Estimates of momentum flux associated with equatorial Kelvin and gravity waves, *J. Geophys. Res.,* this issue.

Schmidlin, F. J., Intercomparisons of temperature, density, and wind measurements from in situ and satellite techniques, Adv. Space Res., *4,* 101–110, 1984.

Schmidlin, F. J., Rocket techniques used to measure the middle atmosphere, *MAP Handb., 19,* 1–28, 1986.

Schmidlin, F. J., H. Carlson, D. Rees, D. Offermann, C. R. Philbrick, and H.-U. Widdel, Wind structure and variability in the middle atmosphere during the November 1980 Energy Budget Campaign, *J. Atmos. Terr. Phys., 47,* 183–193, 1985..

Shiotani, M., J. C. Gille, and A. E. Roche, Kelvin waves in the equatorial lower stratosphere as revealed by Cryogenic Limb Array Etalon Spectrometer (CLAES) temperature data, *J. Geophys. Res.,* this issue.

Smith, S. A., D. C. Fritts, and T. E. VanZandt, Evidence for a saturated spectrum of atmospheric gravity waves, *J. Atmos. Sci., 44,* 1404–1410, 1987.

Spano, E., M. Crochet, and O. Ghebrebrhan, Some characteristics of the matrix used for the full decoding of truncated ranges, in *Solar-Terrestrial Energy Program: Proc. Fifth Workshop of Technical and Scientific Aspects of MST Radar,* B. Edwards (ed.), 439–445, 1991. Available from SCOTEP Secretariat, NOAA/NGDC, Boulder, CO.

Takahashi, M., and T. Kumakura, 1995: Equatorial wave behavior in a three-dimensional sector model: Relation to the simulated QBO-like oscillation and comparison with a T21 General Circulation Model, *J. Atmos. Sci., 35,* 714–722.

Tsuda, T., T. Inoue, D. C. Fritts, T. E. VanZandt, S. Kato, T. Sato, and S. Fukao, MST radar observations of a saturated gravity wave spectrum, *J. Atmos. Sci., 46,* 2440–2447, 1989.

Vincent, R. A., and D. Lesicar, Dynamics of the equatorial mesosphere: First results with a new generation partial reflection radar, *Geophys. Res. Lett., 18,* 825–828, 1991.

Vincent, R. A., and I. M. Reid, HF Doppler measurements of mesospheric momentum fluxes, *J. Atmos. Sci., 40,* 1321–1333, 1983.

Wang, D.-Y., and D. C. Fritts, Evidence of gravity wave-tidal interaction observed near the summer mesopause at Poker Flat, Alaska, *J. Atmos. Sci., 48,* 572–583, 1991.

Young, H. D., Statistical Treatment of Experimental Data, McGraw-Hill, New York, 172 pp., 1962.

Yuan, L., and . C. Fritts, Influence of a mean shear on the dynamical instability of an inertio-gravity wave, *J. Atmos. Sci., 46,* 2562–2568, 1989.

C. D. Fawcett and E. Kudeki, Department of Electrical and Computer Engineering, CSRL MC-229, 1308 W. Main Street, University of Illinois, Urbana, IL 61801. (e-mail: cfawcett@uiuc.edu; erhan@deln.ece.uiuc.edu)

D. C. Fritts, J. F. Garten, and D. M. Riggin, Colorado Research Associates/NWRA, 3380 Mitchell Lane, Boulder, CO 80301. (e-mail: dave@michelangelo.colorado.edu; James.Garten@Colorado.edu; Dennis.Riggin@Colorado.edu)

R. A. Goldberg and G. A. Lehmacher, Laboratory for Extraterrestrial Physics, NASA Goddard Space Flight Center, Greenbelt, MD 20771. (email: goldberg@nssdca.gsfc.nasa.gov)

M. H. Hitchman, Department of Atmospheric and Oceanic Sciences, University of Madison-Wisconsin, 1225 West Dayton St., Madison, WI 53706. (e-mail: matt@adams.meteor.wisc.edu)

R. S. Lieberman, Space Physics Research Laboratory, University of Michigan, Ann Arbor, MI 48109. (e-mail: lieberman@sprlj.sprl.umich.edu)

S. McCarthy and F. J. Schmidlin, Wallops Flight Facility, NASA Goddard Space Flight Center, Code 972, Wallops Island, VA 23337. (e-mail: fjs@osbl.wff.nasa.gov)

I. M. Reid and R. A. Vincent, Department of Physics and Mathematical Physics, University of Adelaide, Adelaide, S. A. 50001, Australia (e-mail: ireid@physics.adelaide.edu.au; rvincent@physics.adelaide.edu.au)

(Received May 10, 1996; revised November 19, 1996; accepted November 25, 1996.)